공학박사 학위논문

# Computational multi-layered holographic display featuring effective resolution enhancement

## 유효 해상도의 향상이 가능한 전산 다층 홀로그래픽 디스플레이

2020년 2월

서울대학교 대학원

전기·컴퓨터공학부

조 재 범

공학박사 학위논문

# Computational multi-layered holographic display featuring effective resolution enhancement

## 유효 해상도의 향상이 가능한 전산 다층 홀로그래픽 디스플레이

2020년 2월

서울대학교 대학원

전기·컴퓨터공학부

조 재 범

# Computational multi-layered holographic display featuring effective resolution enhancement

지도 교수 이 병 호

이 논문을 공학박사 학위논문으로 제출함

2020년 2월


서울대학교 대학원

전기·컴퓨터공학부

조 재 범


조재범의 공학박사 학위 논문을 인준함

2020년 2월

위 원 장: _____ (인)

부위원장: _____ (인)

위 원: _____ (인)

위 원: _____ (인)

위 원: _____ (인)

## Abstract

# Computational multi-layered holographic display featuring effective resolution enhancement

Jaebum Cho
Department of Electrical Engineering and Computer Science
College of Engineering
Seoul National University

This dissertation discusses novel multi-layered holographic displays that can extend the space-bandwidth product (SBP) of the system while minimizing the volume of that. Stacking low-resolution spatial light modulators (SLMs) in the direction of the optical axis not only minimizes the size of the display but also avoids seams caused by the bezel of the SLMs. Since CGHs for multi-layered holographic display cannot be calculated directly, a method to optimize computer-generated holograms (CGHs) for extending SBP of multi-layered holographic displays. The proposed optimization method can be applied regardless of the modulation type of SLM or the number of SLMs. It is demonstrated that multi-layered holographic displays can extend SBP using multiple SLMs.

A fast algorithm to generate ultra-high resolution CGH for multi-layered holographic displays is proposed. It is shown that Fourier typography method can calculate CGHs with ultra-high resolution and high image quality faster than conventional methods. The intermediate pupil function, which can reduce the computational load, is derived by the embedded pupil function recovery (EPRY) technique. By solving the integrated least squares equation with the gradient descent method, the convergence of the optimization can be improved than

the iterative Fourier transform algorithm (IFTA). In addition, it is shown that the proposed algorithm can optimize phase-only CGHs for three-dimensional objects that is difficult to optimize with the IFTA. Through experiments and simulations, it is verified that the proposed algorithm has an advantage in computation speed and image quality over conventional methods.

An optimization method to reduce inherent noises of multi-layered holographic displays is investigated. CGH optimization algorithm for a multi-layered on-axis holographic system that does not require additional relaying optics and can minimize energy loss is proposed. The experiments show that the proposed optical system and the optimization algorithm can effectively eliminate DC noise. A method for compensating CGHs for SLMs with irregular sub-pixel structures is also proposed. The algorithm can be applied to the arbitrary sub-pixel structure and pixel alignment problems of multi-layered holographic displays.

**keywords**: Holographic display, computer-generated hologram, space-bandwidth product, iterative Fourier transform algorithm, digital holography
**student number**: 2013-20888

# Contents

# List of Tables

# List of Figures

# Chapter 1. Introduction

## 1.1 Current issues of holographic display

Virtual reality (VR) and augmented reality (AR) are emerging as next-generation display platforms that will solve limitations of time and space in real human life [1–4]. For truly practical VR/AR displays to be implemented, there are still a few issues, the most important of which is the realization of realistic three-dimensional (3D) images. The currently commercialized 3D displays use a stereoscopic method which utilizes binocular disparity. While the stereoscopic method is the most efficient way to use the resolution capacity of the display, it cannot provide any other visual cues such as the focus cue [5–7]. This means that not only viewers can feel a motion sickness due to the vergence-accommodation conflict (VAC) but also cannot focus actively on what they want to see. Enormous research is underway to address the VAC problem. Some studies show that accommodation cue can achieve in the light-field regime [7–10]. The light-field display that supports focus cue has also been used as vision-correcting displays [11]. A method to realize a focus cue by generating a dense light-field through temporal multiplexing has also been proposed [12]. They approximate the light field to a bundle of rays, as known as light-field. Thus, the light-field displays suffer from low-resolution images due to the diffraction. Volumetric displays have been proposed to overcome these limitations that can image an object on a certain depth. The volumetric displays often use tunable optics that are synchronized with each frame of a display to image the display to a certain depth [13–16]. Instead of a flat display, some volumetric display utilizes floating particles in the air, controlled by optical [17] or acoustic trapping [18]. Since the volumetric displays can express all 3D cues humans can perceive, and they do

not have eye safety issues due to the speckles of coherent light [19], they are emerging as the biggest competitor of holographic displays, recently. However, they always require complicated devices for temporal multiplexing. Moreover, the volumetric display is difficult to represent an image occluded by another image in front of it despite efforts to alleviate the occlusion problem [13]. Since holographic displays provide 3D images that are physically close to nature's way, they are one of the ultimate 3D display candidates. Theoretically, holographic images, most natural 3D images, can be represented by the coherent light source and the SLM that can modulate the amplitude and phase of the light source independently, but some challenges are remained to be solved in the holographic display.

First, there are only amplitude and phase-only type SLMs that cannot modulate amplitude and phase independently. This limitation can cause critical problems. For example, phase-only SLMs cannot represent an image at its own depth. To overcome this limitation, encoding techniques that can convert complex hologram into amplitude or phase-only hologram are proposed [20–26], and similarly, the study of complex modulation by using an additional optics for combining some pixel has also been conducted [27,28]. However, these methods have a limitation to reduce the pixel pitch. Fundamental ideas to develop a complex modulation in a pixel level are also proposed by using meta-surface [29] and bi-material with thermal modulation [30]. However, the complex modulator is still a challenging goal.

Secondly, the speckle noises caused by the coherent light source are also a significant issue of holographic displays. Speckle noise not only degrades image quality but can also damage human eyes due to the high energy spots that can be generated statistically. For averaging out the speckle noises, temporal multiplexing technique has been widely studied [31–41]. Recently, a speckle

reduction method without temporal multiplexing is also proposed [42]. Speckle noise is still an essential issue in holographic displays because the trade-off between speckle contrast and image resolution has not yet been untangled.

Lastly, the most severe issue is a lack of SLM resolution. The resolution may refer to both the number of pixels and the pixel size. In terms of holographic display, both meanings are important. The pixel size, as known as the pixel pitch, is related to the field of view (FOV) in the Fourier type hologram. With the smaller pixel pitch, the wider FOV can be achieved. The total size of displays can be calculated by the product of the number of pixels and the pixel size. The size of displays is related to the maximum 3D image size that the display can represent in the Fourier type hologram. Thus, the product of the image size and the FOV, called space-bandwidth product (SBP), is proportional to the number of pixels. The SBP means the total capacity of the holographic displays [43]. For example, the most advanced SLM in the market has 4K resolution and $3.74\,\mu\mathrm{m}$ pixel pitch, recently. The maximum image size that the SLM can represent is about $14.4 \times 8.1\,\mathrm{mm}$ in the SLM plane, and FOV is about $8.18^{\circ}$. Not only the image size but also the FOV is not sufficient for a practical holographic display. To overcome the resolution limit, temporal multiplexing techniques using fast-scanning optics such as mirror galvanometer is proposed [44–54].These systems require ultra-fast mechanical parts synchronizing with SLM. Spatial multiplexing techniques are also proposed [55] by tiling multiple SLMs. However, the proposed holographic display has a large system due to the low pixel density of tiled SLMs. Recently, the novel methods that can break SBP limitation using random optics is proposed [56, 57]. Certainly, the proposed holographic display has the wider FOV and the larger imaging region, but at the expense of image quality. They cannot control noises. Eventually, the overall information capacity of holographic displays is proportional to the number of pixels.

In this dissertation, the novel method to extend SBP of holographic display is proposed using multiple SLMs. A method to stack multiple SLMs to the direction of the optical axis to keep the form-factor compact while increasing the effective number of pixels. The proposed holographic display can distribute the entire resource, depending on how CGH is calculated. For example, additional pixels from other SLMs can be used for increasing effective resolution or can be used to encode complex holograms for amplitude and phase-only SLMs.

## 1.2 Motivation and purpose of this dissertation

As mentioned in the introduction, the number of pixels which are proportional to the SBP is the most critical factor to holographic displays. Strictly speaking, the pixel size is also important because the additional effort is required to control of trade-off relation between image size and FOV. For example, an LCD display with 8K resolution has a relatively large SBP, but it can provide an only large image with tiny FOV. An additional bulky optics to demagnify the large image is required to secure the reasonable FOV. In other words, to build a practical holographic display without additional optics, a high density of display pixels is required. However, there are physical limitations to developing pixels as small as enough for practical holographic displays.

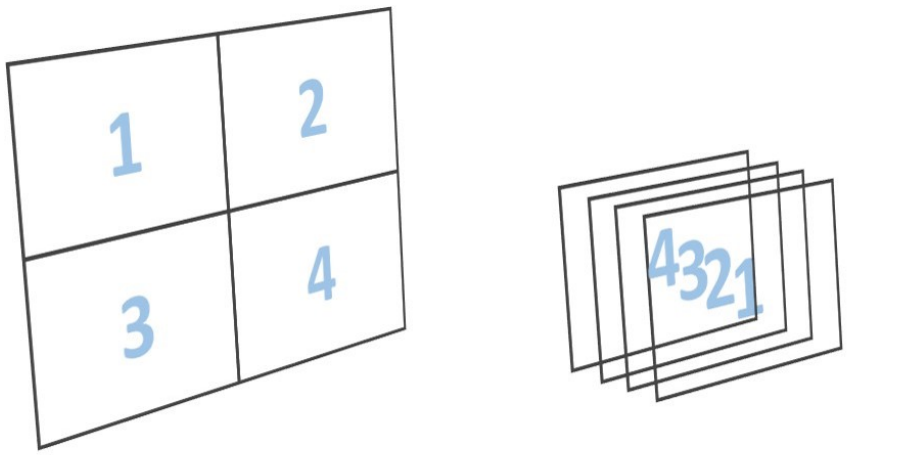


Figure 1.1 The concept of multi-layered holographic display.

In this dissertation, a system-based solution to this high-density pixel problem is proposed. The multi-layered holographic displays is a novel method to achieve a high-density pixel structure while minimizing the size of the system,

as illustrated in Fig. 1.1. The problem of the multi-layered display is that CGHs for this system cannot be computed directly, and the CGH optimization technique is a key to develop the system. This dissertation mainly aims at the development of the CGH design method for the multi-layered holographic displays. Fortunately, the CGHs of multi-layered hologram has a large degree of freedom to be optimized for the purpose. The CGHs can be optimized to extend SBP for implementing effectively high-density pixel and can be optimized to the display work as a complex modulator. It is also expected that the inherent noises of SLMs could be eliminated with the properly optimized CGHs, and additional functions such as high dynamic range (HDR) can be implemented.

The multi-layered holographic display has great potential as the next generation holographic display. The multi-layered display is the first step towards a volumetric hologram display, and the study of the volumetric hologram display is an unknown area that has rarely been studied.

## 1.3 Scope and organization

In Chapter 1, the current issues in research of holographic displays are introduced, and the importance of this research is claimed.

In Chapter 2, the CGH design method for layered displays is also proposed. The number of pixels limits the amount of information that a holographic display can represent, but there is also a limit to the pixel density becoming higher. By stacking displays, the number of pixels can be increased, maintaining the form-factor. The CGH optimization method for exploiting the surplus pixels is proposed and demonstrated.

In Chapter 3, the CGH design method via Fourier ptychography is introduced. The problems using Fourier ptychography to generate CGH are introduced, and the solution to relax the convergence condition is proposed. The proposed algorithm can convert light field data into complex hologram minimizing the loss of resolution. Compared to the conventional design methods, the proposed algorithm has an advantage in resolution, computation load, and visual effects, including occlusion.

In Chapter 4, the DC noise-free on-axis holographic display is introduced. The purpose of this study is to eliminate the DC noise of holographic display. Generally, the off-axis method is widely used to achieve the same purpose. It is hard to separate DC noise in an on-axis system because the signal from the display is overlapped with DC noise. CGH can be optimized to have a signal to avoid DC noise using the two-step iterative Fourier transform algorithm. The limitation of the proposed method is explained, and the experimental results are demonstrated.

CGH design method for holographic display with irregular structure. Since commercialized LCDs with high pixel density and resolution usually have the irregular pixel structure which arranges the pixels in a zigzag shape, it is hard

to use these LCDs as a holographic display. Using the proposed method, this high-resolution LCD can be used as a holographic display. Finally, concluding and future work remark in Chapter 5.

# Chapter 2. Multi-layered holographic display for extending spatial-bandwidth product

## 2.1 Introduction

The resolution of a spatial light modulator (SLM) is the most important factor for realizing practical holographic display. Rigorously speaking, a concept of the space-bandwidth product (SBP) is appropriate to show the total amount of information that the display can represent. In Fig. 2.1, the intuitive concept of SBP in Fourier holographic displays is represented. The maximum image size is inverse proportional to the pixel size, and the field of view (FOV) is proportional to the entire size of the display. The display size is the product of the pixel pitch and the number of pixels of the display. Thus, the product of image size and FOV is also proportional to the number of pixels. This also means that the image size and FOV are in a trade-off relation, and both factors shares one resource, the number of pixels. As mentioned above, temporal and spatial multiplexing methods are widely studied to extend SBP of the holographic displays. Multiplexing methods suffer from large form-factor with mechanical parts for multiplexing. Methods using random optics do not need any mechanical parts for extending SBP. They can break the SBP limit in the traditional definition of SBP, but the problem is that noise is not considered in SBP. The effective number of pixels should be increased to extend SBP without noise. Therefore, in this chapter, a multi-layered holographic display is proposed to increase the number of effective pixels minimizing the display system.

Originally, the concept of the layered display is proposed for light-field displays. At first, the layered display is started as the parallax barrier display. In

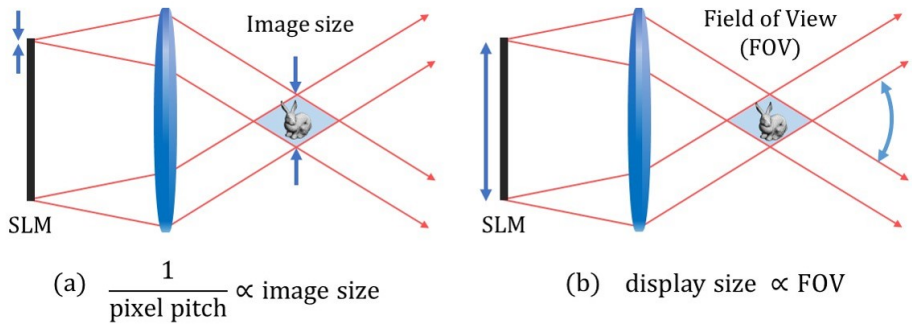


Figure 2.1 Change in holographic display performance according to SLM pixel specifications. (a) The image size and the pixel pitch are in inverse proportion, and (b) the FOV is proportional to the entire display size.

this study, the second layer is utilized as the content-adaptive parallax barrier to improving the performance of the displays [58]. The generalized version with temporal multiplexing and directional back-light is also proposed [59]. Furthermore, the additive layered display is proposed for augmented reality displays [60]. The concept of computational display that can improve the performance by optimized contents arises from these studies. However, these methods have a limitation on their image quality because the light-field display does not consider the diffraction of light.

In the holography, it is well known that volumetric holograms can handle much more information than thin holograms. Various images can be multiplexed for the angle of incident light using the volumetric hologram [61]. Recently, the multi-layered holographic system is utilized for artificial neural networks [62, 63]. Although it is challenging to implement non-linear activation function in all-optical networks, these studies show that the multi-layered system can calculate linear operations.

In this chapter, the architecture of a multi-layered holographic display is

proposed. It is shown that the multi-layered holographic display can extend the SBP, and can calculate linear operations such as encoding the amplitude-only or phase-only holograms into complex holograms.

## 2.2 Optimization of computer-generated hologram for multi-layered holographic displays

The geometrical setup of the multi-layered holographic display is shown in Fig. 2.2(a). For simplicity, only two SLMs are used in Fig. 2.2(a). The two SLMs are cascaded in parallel with distance of $z$, and two CGHs for each SLM are $\mathbf{a}$ and $\mathbf{b}$, respectively. The target field is in the observation plane $\mathbf{c}$, and is behind $z$ in the second SLM. Note that the sampling number of SLMs, $N_x \times N_y$, is twice larger than the resolution of SLMs, $m_x \times m_y$, because the bandwidth of the signal is expected to be doubled passing through the two SLMs. From the SLM $\mathbf{a}$ to the observation plane $\mathbf{a}$ can be modeled with operation matrices, as shown in Fig. 2.2. The matrix $\mathbf{I}$ is an interpolation matrix which double up the resolution of $\mathbf{a}$. The box-shaped kernel interpolates by copying neighboring pixel values without any calculations. After the interpolated $\mathbf{a}$ is propagated to the second SLM, the second CGH, $\mathbf{a}$ is multiplied. Here, $\mathbf{b}$ is also interpolated by the matrix $\mathbf{I}$. Then, the field is propagated to the plane $\mathbf{c}$. For the propagation matrix, the angular spectrum method is used [64, 65]. Note that there are two unknown variables, $\mathbf{a}$ and $\mathbf{b}$, and these two variables cannot be optimized simultaneously. Therefore, only one of $\mathbf{a}$ and $\mathbf{b}$ should be optimized at a time, and the other is set to constant.

Then, two least squares equations can be induced for $\mathbf{a}$ and $\mathbf{b}$, as shown in Fig. 2.3. In Fig. 2.3(b), the equation for $\mathbf{b}$ can be derived by commutative law. Since these equations are bi-convex in $\mathbf{a}$ and $\mathbf{b}$, it can be solved alternately for $\mathbf{a}$ and $\mathbf{b}$ [66]. There are various iterative solvers for these equations. In this dissertation, the gradient descent (GD) method is used. The GD method is straightforward mathematically, making it easy to apply various constraints and also requires only the conjugate transpose of the system matrices to calculate the gradient of the system matrices. The most conjugate transpose of

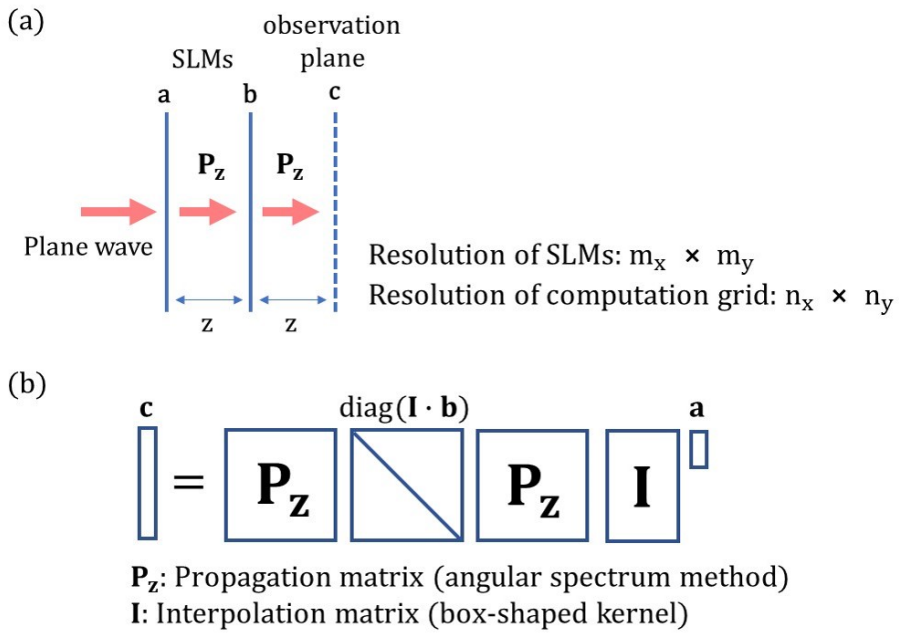


Figure 2.2 (a) Geometrical setup for the multi-layered holographic displays, and (b) diagram of the modeling equation.

the operators for lossless linear optical systems are well defined. For example, the conjugate transpose of the Fourier transform matrix is the inverse Fourier transform matrix, and the conjugate transpose of the interpolation matrix $\mathbf{I}$ is an average pooling operator. The two cost functions can be organized in Eq. (2.1).

(a) Equation for $\mathbf{a}$

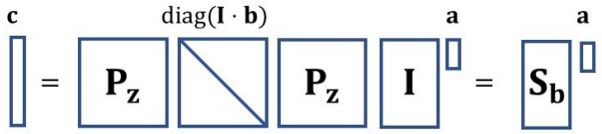


(b) Equation for $\mathbf{b}$

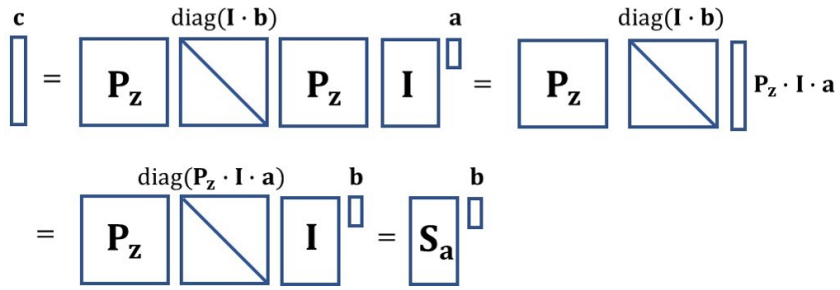


Figure 2.3 Matrices and vectors diagram of least squares equations for (a) $\mathbf{a}$, and (b) $\mathbf{b}$.

The gradients of Eq. (2.1) are defined by

$$\begin{aligned} f(\mathbf{a}) &= \|\mathbf{t} - \mathbf{S_b a}\|_2^2 \\ f(\mathbf{b}) &= \|\mathbf{t} - \mathbf{S_a b}\|_2^2 \end{aligned} \tag{2.1}$$

where $\mathbf{S_a}$ and $\mathbf{S_b}$ are system matrices induced for the fixed $\mathbf{a}$, $\mathbf{b}$, respectively. $\mathbf{t}$ is a target complex hologram to reconstruct, and the $\dagger$ means the conjugate transpose.

$$\begin{aligned}\nabla f(\mathbf{a}_i) &= 2\mathbf{S}^{\dagger}{}_b\left(\mathbf{S}_b\mathbf{a}-\mathbf{t}\right)\\ \nabla f(\mathbf{b}_i) &= 2\mathbf{S}^{\dagger}{}_a\left(\mathbf{S}_a\mathbf{b}-\mathbf{t}\right)\end{aligned} \tag{2.2}$$

Step sizes of each iteration can be calculated as Eq. (2.3) [67].

$$\begin{aligned}\alpha &= \frac{\nabla f^{\dagger}(\mathbf{a})\cdot\nabla f(\mathbf{a})}{2\nabla f(\mathbf{a})\mathbf{S}^{\dagger}\mathbf{S}\nabla f(\mathbf{a})}\\ \beta &= \frac{\nabla f^{\dagger}(\mathbf{b})\cdot\nabla f(\mathbf{b})}{2\nabla f(\mathbf{b})\mathbf{S}^{\dagger}\mathbf{S}\nabla f(\mathbf{b})}\end{aligned} \tag{2.3}$$

The pseudo code for optimizing process is described in Algorithm 2.1. Note that the algorithm is easily expandable for the number of the SLM layers.

**Algorithm 2.1** Optimization CGHs for multi-layered holographic display

**Initialize:**

$i \leftarrow 0$

$\mathbf{a_o} \leftarrow$ initialized to random complex number

$\mathbf{b_o} \leftarrow$ initialized to random complex number

**repeat**

$\nabla f(\mathbf{a}_i) \leftarrow 2\mathbf{S}_b\left(\mathbf{S}_b\mathbf{a}_i-\mathbf{t}\right)$
$\alpha \leftarrow \dfrac{\nabla f^{\dagger}(\mathbf{a}_i)\cdot\nabla f(\mathbf{a}_i)}{2\nabla f(\mathbf{a}_i)\mathbf{S}^{\dagger}\mathbf{S}\nabla f(\mathbf{a}_i)}$
$\mathbf{a}_{i+1} \leftarrow \mathbf{a}_i - \alpha\cdot\nabla f(\mathbf{a}_i)$

$\nabla f(\mathbf{b}_i) \leftarrow 2\mathbf{S}_a\left(\mathbf{S}_a\mathbf{b}_i-\mathbf{t}\right)$
$\beta \leftarrow \dfrac{\nabla f^{\dagger}(\mathbf{b}_i)\cdot\nabla f(\mathbf{b}_i)}{2\nabla f(\mathbf{b}_i)\mathbf{S}^{\dagger}\mathbf{S}\nabla f(\mathbf{b}_i)}$
$\mathbf{b}_{i+1} \leftarrow \mathbf{b}_i - \beta\cdot\nabla f(\mathbf{b}_i)$

$i \leftarrow i+1$

**until** converge

The amplitude or phase-only constraint also can be adopted to the proposed algorithm. Although the layered display requires the expense of resolution for

complex modulation, the layered display can reconstruct the complex hologram only using amplitude or phase-only SLMs. The constraint can be implemented easily by adding the constraint that forces the solution $\mathbf{a}$ and $\mathbf{b}$ to each type of value. After updating $\mathbf{a_i}$ and $\mathbf{b_i}$ for each iteration, the absolute of the updated value will hand over to the next iteration, as shown in Algorithm 2. With these constraints, $\mathbf{a}$ and $\mathbf{b}$ are forced to converge to the amplitude or phase-only solution.

**Algorithm 2.2** Optimization of amplitude/phase-only CGH

**Initialize:**

$i \leftarrow 0$

$\mathbf{a_o} \leftarrow$ initialized to random number

$\mathbf{b_o} \leftarrow$ initialized to random number

**repeat**

$\nabla f(\mathbf{a}_i) \leftarrow 2\mathbf{S}_b\left(\mathbf{S}_b\mathbf{a}_i - \mathbf{t}\right)$

$\alpha \leftarrow \dfrac{\nabla f^{\dagger}(\mathbf{x}_i)\cdot\nabla f(\mathbf{x}_i)}{2\nabla f(\mathbf{x}_i)\mathbf{S}^{\dagger}\mathbf{S}\nabla f(\mathbf{x}_i)}$

$\mathbf{a}_{i+1} \leftarrow |\mathbf{a}_i - \alpha\cdot\nabla f(\mathbf{a}_i)|$ or $\mathbf{a}_{i+1} \leftarrow \exp\left\{j\angle\left(\mathbf{a}_i - \alpha\cdot\nabla f\left(\mathbf{a}_i\right)\right)\right\}$

{amplitude/phase-only constraint}

$\nabla f(\mathbf{b}_i) \leftarrow 2\mathbf{S}_a\left(\mathbf{S}_a\mathbf{b}_i - \mathbf{t}\right)$

$\beta \leftarrow \dfrac{\nabla f^{\dagger}(\mathbf{x}_i)\cdot\nabla f(\mathbf{x}_i)}{2\nabla f(\mathbf{x}_i)\mathbf{S}^{\dagger}\mathbf{S}\nabla f(\mathbf{x}_i)}$

$\mathbf{b}_{i+1} \leftarrow |\mathbf{b}_i - \beta\cdot\nabla f(\mathbf{b}_i)|$ or $\mathbf{b}_{i+1} \leftarrow \exp\left\{j\angle\left(\mathbf{b}_i - \beta\cdot\nabla f\left(\mathbf{b}_i\right)\right)\right\}$

{amplitude/phase-only constraint}

$i \leftarrow i + 1$

**until** converge

## 2.3 Numerical results

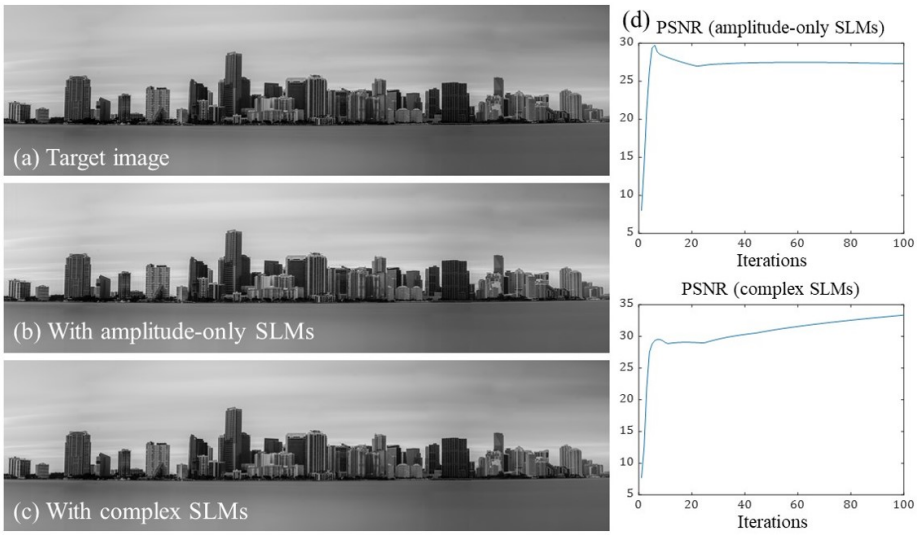


Figure 2.4 (a) Target image for the optimization, the reconstructed images from the optimized CGHs with (b) two amplitude-only SLMs and (c) two complex SLMs, and (d) their convergence graphs.

The figure 2.4(b) shows the reconstructed image from the optimized CGHs for the amplitude-only SLMs. The resolution of SLMs is $1080 \times 1920$, the pixel pitch of SLMs is $8.5\,\mu\mathrm{m}$, and $z$ the distance between SLMs is $5\,\mathrm{mm}$. Note that the resolution of the target hologram is $1080 \times 3840$, which is twice larger than the SLMs, and the horizontal sampling interval is half that of the SLMs. In this case, due to the amplitude-only SLMs, the information capacity of the system is not sufficient to represent the complex target hologram. This lack causes the noises on the reconstructed image, and the Peak Signal-to-noise ratio (PSNR) is lower than using the complex SLMs, as shown in Fig. 2.4(d).

The figure 2.4(c) shows the numerical result for the complex SLMs. The

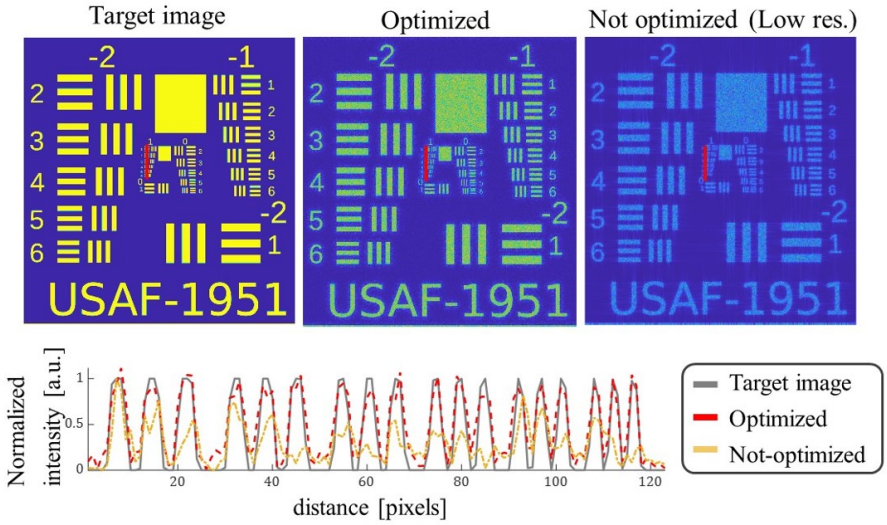


Figure 2.5 Numerical results with the USAF resolution chart using four SLMs.

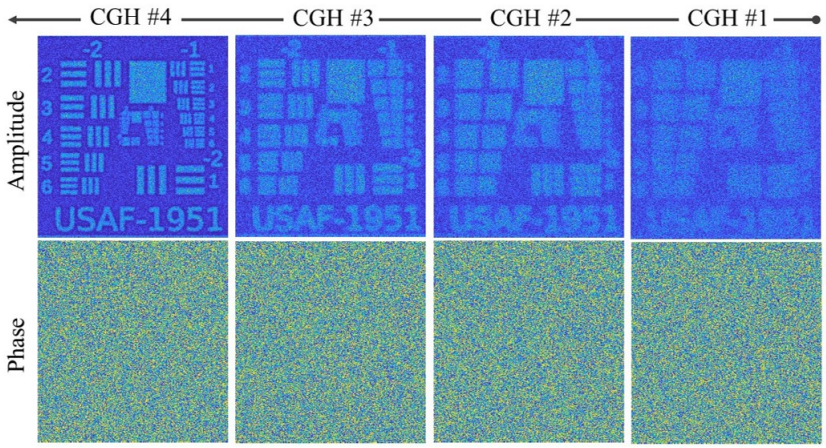


Figure 2.6 The optimized holograms for each SLMs.

same resolutions of target and SLMs are used with the previous result. In this case, the total number of pixels and the required degree of freedom are matched.

In Fig. 2.5, four complex SLMs with $500 \times 530$ resolution are used. The effective number of pixels is the same as the target hologram resolution. The resolution of the target image is $1000 \times 1060$, the distance $z$ between the SLMs is $1\,\mathrm{mm}$, and the sampling interval is $6\,\mu\mathrm{m}$. In Fig. 2.5(d), the cross-sectional profiles of the target image, the reconstructed image from the multi-layered display (optimized), and the interpolated image (not optimized), which is measured along red lines are compared. The numerical results show that the reconstructed image from the multi-layered holographic display is well-matched with the target image. In Fig. 2.6, the optimized four CGHs with $500 \times 530$ resolution are represented. Note that the fourth CGH is closer to the target image plane, and the target image pattern is clearly observable in the amplitude of the fourth CGH. The first CGH farther from the target image shows the blurry amplitude patterns.

## 2.4 Conclusion

In this chapter, the architecture of the multi-layered holographic displays is proposed, and the CGH optimization method is also proposed. Due to the large DOF if the proposed holographic display, the multi-layered display can perform various tasks depending on how the CGH is optimized. It is shown that the multi-layered holographic displays can increase the effective resolution of the display. By adding constraints for modulation type of SLMs, the multi-layered displays can work as complex modulators with amplitude-only or phase-only SLMs. The proposed method is scalable for the number of SLM layers. Since transpose or conjugate transpose of the operations in the Fourier optics are well defined, the system matrix is not required to declare explicitly. This feature allows large-scale optimization with high-resolution SLMs. By increasing the number of SLMs, it is expected that the multi-layered display can be closer to the volumetric holograms, which can perform various optical tasks.

# Chapter 3. Efficient method to synthesize high resolution computer-generated hologram for multi-layered holographic displays with extended spatial-bandwidth product

## 3.1 Introduction

In Chapter 2, it is demonstrated that the multi-layered holographic displays can represent the high resolution of computer-generated holograms (CGHs). In this chapter, an efficient CGH generation method for the high-resolution holographic displays, such as the multi-layered holographic displays, is proposed and investigated.

Since hologram is a technology for representing 3D images, the goal of the holographic contents should be realistically reproducing the real scene. However, a tremendous amount of calculation is required to reproduce the interactions between light and objects in nature. Recent CGH research has focused on reducing computation load while maintaining the quality of three-dimensional images. The method of calculating CGH can be largely divided into a point cloud, polygon, layer, and multi-view methods according to the basic unit of calculation.

The point cloud method decomposes the target objects into points in 3D space. A thin lens profile can approximate the unit holograms of each point. The total hologram can be calculated by superposing all of these unit holograms. The point cloud method is the most straightforward and most intuitive and is widely used for the practical hologram calculation. However, the amount of cal-

culation is enormous because many points are required to present a 3D surface. Therefore, the lookup table (LUT) method has been widely studied to reduce the computation load by recycling the lens profiles already calculated [68, 69]. A wavefront-recording plane (WRP) method has also been proposed to reduce the computation region by locating the position of hologram recording plane to the object points [70–72]. The polygon-based method decomposes the target surface into polygons or triangles. In this case, the unit polygon is already a 3D object, so it is not straightforward to calculate the unit hologram. There are two methods, analytic and numerical method, to calculate the unit polygon hologram. Fully analytic Fourier transformation of an arbitrary triangle has been proposed and utilized to calculate the unit hologram [73]. This method can directly calculate the unit hologram without Fourier transform. In the other study, they calculate the unit hologram by remapping the values in the Fourier domain [74]. The remapping process needs Fourier transform and interpolation operation, which has a high burden to compute. These methods can handle the conventional polygon-based computer graphics (CG) object directly. Textures and material rendering of object surfaces also can be implemented like in CG [74, 75]. This is a significant advance for the expression of photo-realistic images. In the layer-based method, the sliced layers for quantized depths are the unit [76]. Instead of calculating points at all depths, points at similar depths can be approximated to one plane. Propagation between parallel planes well established by Fourier transform, so the computation time to do integral can be saved. As the depth range of object increases, the calculation load also increases, and the gaps between the layers can be observed from a different viewing angle. A method of calculating a local hologram for each viewing angle and tiling it in the Fourier domain has been proposed to avoid this defect [77]. Multi-view-based methods, as known as holographic stereograms, generate hologram using im-

ages from different viewing angles. Ray sampling (RS) method approximates the local plane wave as a light ray [78]. This method is simple and fast and easy to implement, rendering issues such as occlusion, texture, and materials using the conventional CG renderer. The tiling of Fourier transformed elemental images is the whole process of generating holograms. However, ray sampling methods suffer from the spatial resolution issue. While the image resolution of the other methods introduced above is determined by the numerical aperture (NA) of the optical system, ray sampling methods cannot utilize full NA. In most multi-view methods include the RS method, the calculation field is divided into non-overlapping small areas, and the calculation is independent with adjacent areas. These small areas are called hogel. The hogel-based methods are usually faster than other methods thanks to non-overlapping calculation areas, but it trades spatial resolution off instead [79]. Non-hogel-based method and overlap-add stereograms (OLAS) are developed to overcome these limitations [80, 81]. In these methods, the inverse Wigner distribution function (WDF) is utilized to interconnect between wave and light-field approaches. These methods can alleviate a spatial resolution issue but still suffer from a large computation load.

In Fig. 3.1, schematic diagrams to explain the difference between each CGH generation algorithm are represented. All holograms can be decomposed by the superposition of multiple plane waves by Fourier transform, and the resolution and quality of hologram can be defined by the number of the planes waves [64]. For the point cloud CGH and the polygon CGH, the full basis of plane waves is used, and there are no resolution and quality issues in these methods. On the contrary, in the holographic stereograms (HS), only a small set of localized plane waves are used. Therefore, the HS method suffers from the resolution problems. The overlap-add stereograms (OLAS) use the full set of localized plane waves. Thus, the size of the localized region is an important factor in

deciding the resolution and quality of OLAS CGH.

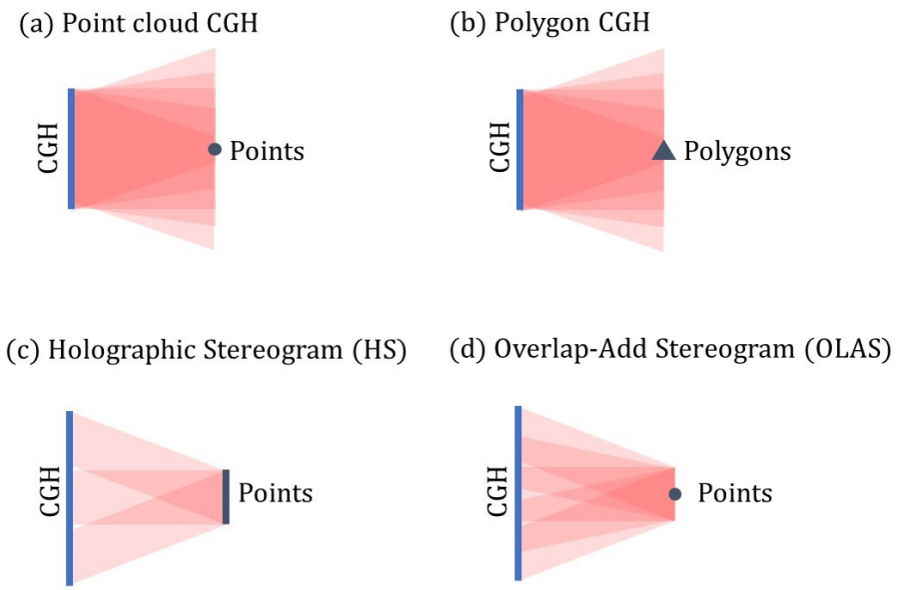


Figure 3.1 Comparison of CGH generation methods.

Table 3.1 shows the algorithm comparison for the resolution, computation load, ease of applying visual effects, and the type of input data. No algorithm can show robust quality with short computation time.

Fourier ptychographic approach is also proposed to reduce calculation load [82]. With Fourier ptychographic method, localized multi-view images are used similar to the RS method, but the overlapping information is exploited to generate CGH so that the spatial resolution issue can be relaxed. The Fourier ptychographic approach has many potentials in terms of computation time, ease of rendering, and quality of results, but these potentials are not fully revealed in the previous study. The Fourier ptychographic method is based on a coherent light regime. This means multi-view images only taken within partially or fully coherent light sources can be used. This significant difference is ignored in the

Table 3.1 Comparison of CGH synthesis algorithms

| | HS | OLAS | Polygon | Point |
|---|---|---|---|---|
| **Resolution** | low | high | high | high |
| **Computation** | low | high | high | high |
| **Visual effects** | easy | easy | hard | hard |
| **Input data** | LF | LF-D | 3D | 3D |

previous study, and the quality of results is severely degraded. In this chapter, the Fourier ptychographic method will be revisited and analyzed.

Ptychography is developed and studied as a phase retrieval method for imaging applications. Ptychography method can achieve a larger field of view (FOV) than its optical FOV without losing the resolution by processing multiple diffraction patters from the sample [82, 83]. The multiple diffraction images are acquired by translating a sample or camera side by side. The overlapping regions between adjacent images are the key constraints to reconstruct the whole image. The ptychography generally uses Gerchberg-Saxton (GS) algorithm as a phase retrieval algorithm [83], and the overlapping regions work as constraints. The diffraction images are used as amplitude support at the recording plane, and the phase profile at the recording plane left a degree of freedom to be optimized. The updated local image at the recording plane can be back-propagated to the sample plane, and the local profile at the sample plane also can be updated. For the next adjacent image that shares a portion of the FOV, the same process is repeated. Fourier ptychography uses support images that confined in the spatial frequency domain, not in the spatial domain. Instead of moving the sample or camera, the images confined in the Fourier domain can be obtained by adjusting the incident angle of illumination. The algorithm begins with an initial guess

of the whole Fourier domain of the sample. By the windowed inverse Fourier transformation, the localized guess image can be obtained in a spatial domain. Like conventional ptychography, the phase profile of the image remains a degree of freedom (DOF), and the amplitude profile will be updated to the measured image. The size and location of the windows are determined by the angle of illumination and numerical aperture (NA) of the imaging system. In practice, incident angle varying light source is achieved using a light-emitting diode (LED) array for a light source of microscopy [84]. The image localized in the Fourier domain can be considered as multi-view images looking from different angles. Intuitively, the Fourier transform of the object field can be considered as far-field of it, and the windows for localization can be considered as an aperture such as a pupil of humans or cameras to observe it, respectively. Rigorously, in the case of Fourier ptychography, the system is lens-less, so the localized image should be a sub-image with no perspective. The conventional CG can render the sub-images easily, and the rendered sub-images might be used as support images instead of measured images for generating CGH. However, the problem is that CG is based on light ray-based model. Note that also CG rendering is inspired by light behavior of nature, but many rendering techniques do not rely on physics. Therefore, It is challenging to consider the effect of coherent light such as speckle and diffraction in CG rendering. Instead of solving the problem with CG rendering, an intermediate filter for relaxing the coherent effects and energy redistribution method is used and analyzed in this dissertation.

## 3.2 Generation of hologram via Fourier ptychographic method

### 3.2.1 Overview of Fourier ptychography

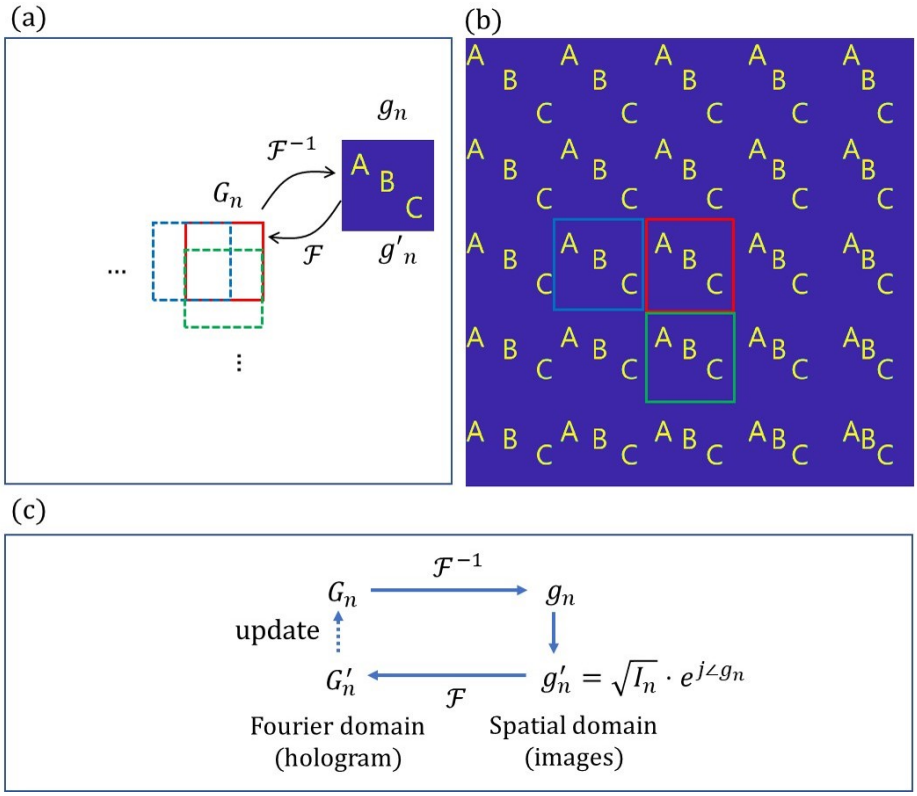


Figure 3.2 (a) Schematic diagram of Fourier ptychography, (b) the target sub-images $I_n$ for each sub-region, and (c) workflow diagram of Fourier ptychography.

In this chapter, the workflow of the proposed method is described. First, the local images to be used as modulus constraints should be created. Unlike the conventional Fourier ptychography, the local images cannot be measured, so it

must be created. The local images are orthographically projected images in a particular viewing angle, which is called sub-images. The viewing angle is determined by the dominant spatial frequency of the confined area. In this study, the sub-images are generated by MATLAB from polygon-based 3D models. Note that the created sub-images cannot be physically equal with the measured images in real. There are no diffraction and blur effects for their depth, and no speckles represented in the sub-images. These issues will be discussed in the later chapters. The workflow of the optimization algorithm is described in Fig. 3.2. First, an initial guess of the entire Fourier hologram is needed as begins. Usually, the central sub-image is used as the initial guess. Random complex field, random phase field, and uniform values can be used as the initial guess for their applications. Second, a selected small local region within the initial guess is inverse Fourier transformed. Note that the intensity of the inverse Fourier transformed sub-hologram should be matched with the target sub-image. There are several algorithms to achieve it. For example, the GS algorithm is the most intuitive algorithm to understand. By GS algorithm, the amplitude of the local profile is replaced with the amplitude of the target sub-image as

$$g_n' = \sqrt{I_n} e^{j\theta_n}, \tag{3.1}$$

where $I_n$ is the target sub-image and $\theta_n$ is the phase angle of $g_n$. The $g_n'$ is Fourier transformed again to the angular spectrum domain, and the confined region of the entire holograms is updated with this profile. Third, the next local region is selected as the next $G_n$. Note that the ratio of the overlapping region between the previous region and the newly selected region to the sub-region is the critical condition to assure the convergence of an algorithm. A more than 70% overlap ratio is usually used to guarantee convergence. These steps are

repeated until all target sub-images update the entire hologram, and these iterations are repeated until the convergence criteria satisfied. The order of selecting the sub-regions may vary depending on the situation and purpose, and it is crucial when using algorithms that update local regions sequentially like the GS algorithm. As mentioned above, the overlaps affect the next update. In most applications, natural images are dealt with, and most natural images have essential information in the low-frequency band. Therefore, the spiral order from the center of the spectrum is used.

### 3.2.2 Geometrical characteristic of target sub-images

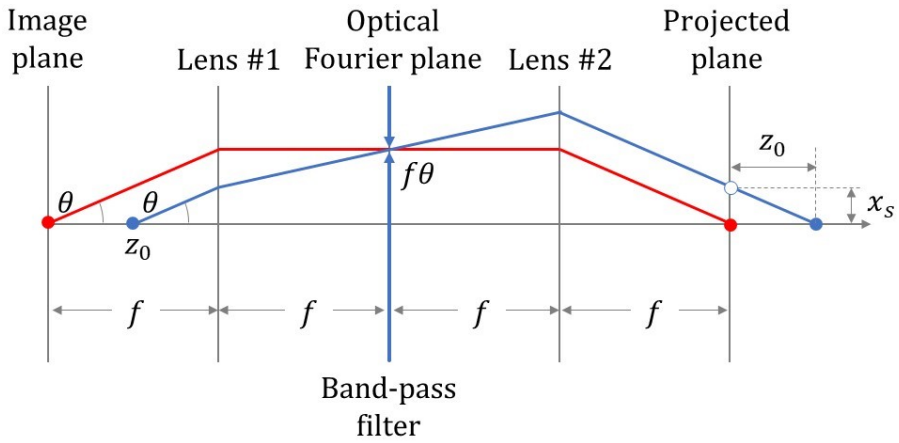


Figure 3.3 Band-pass filtered images in Fourier domain have the same geometrical characteristic with the traditional sub-images.

Unlike conventional Fourier ptychography, which aims at imaging, the proposed algorithm, which aims at holographic contents, must artificially generate target sub-images. Fig 3.3 can explain the geometrical characteristic of the target sub-images. In Fig. 3.3, the red and blue dot s are located at different depth.

The red one is at the origin, and the blue one is at a distance $z_0$. These dots are imaged by a $4f$ imaging system with a band-pass filter on the Fourier domain. If this light field is confined to a singe of frequency in Fourier plane, light rays incident at a specific angle can be passed through the filter. In practice, the band-pass filter has a specific bandwidth. The light rays passing through the filter will have a specific angle range, and the blue dot will be blurred at the projected plane due to this effect. In Fig. 3.3, only chief rays are plotted. After passing through the $4f$ imaging system, the dots are imaged at the exact same location. At the projection plane to record sub-image, the red dot is placed the same location, but the blue dot is shifted by

$$x_s = z_0\theta_x = z_0\lambda u_x, \tag{3.2}$$

where $\lambda$ is a wavelength, and $u$ is the central frequency of the filtered spectrum. When filtering frequency is varying, images are shifted depending on only the depth, $z_0$. This result is the same as the meaning of the traditional orthographic sub-image of an integral imaging [85].

Using commercial computer graphics (CG) rendering programs include MATLAB, sub-images can be rendered without the pseudoscopic problem. In Fig. 3.3, the schematic diagram of the sub-image recording setup is depicted. The setup is expressed with two axes only for simplicity. Note that the setup has three axes, including y-axis. Suppose that sub-image is required for nth sub-region, and the central frequency of the nth sub-region is $\mathbf{u_n}$. Then, the projection direction vector can be defined by

$$\mathbf{k}_n = 2\pi\mathbf{u}_n = 2\pi\left(\frac{\sin\theta_x}{\lambda}, \frac{\sin\theta_y}{\lambda}\right) \tag{3.3}$$

The recording plane should be parallel with the hologram plane, and the origin of the plane should be aligned along the direction of the projection. The location of the recording plane along the z-axis is not defined at a certain depth because the sub-images are orthographic.

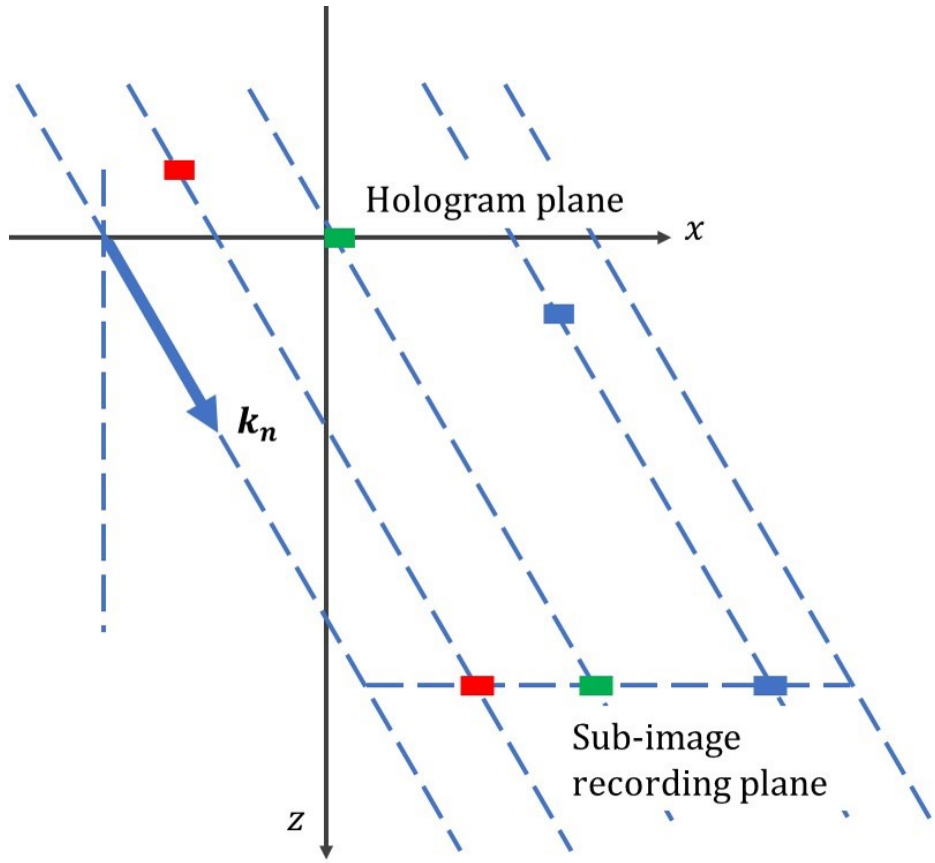


Figure 3.4 Schematic diagram of geometrical setup for the sub-images.

For real scenes, the sub-images cannot be acquired directly. After a light field camera acquires the elemental images, it should be converted into sub-images considering the pseudoscopic problem [86].

### 3.2.3 Determine the size of sub-region

In Fig. 3.5, the generated sub-images and the extracted sub-images from a real hologram are compared. Since the target object has only three depths, the sub-images can be calculated by superposing of shifted each depth of image. The real hologram generated by angular spectrum method. After random phase is multiplied to three objects at their depth position and propagated or back-propagated to the hologram plane. The hologram is divided in five by five regions in their Fourier domain, and the sub-images are calculated by inverse Fourier transformation of each region. First, it can be confirmed that the geometrical position and shape of sub-images are well matched. However, the speckle noise and blur effect due to the out-of-focus cannot be observable in the generated sub-images. These difference affects to the quality of result image significantly. The blur effect can be reduced by setting a size of sub-region properly.

Typically, an arbitrary point source is spread out while propagating, as shown in Fig. 3.6. Here, the resolution of the sub-region can be adjusted to be indistinguishable from the diffracted point source. The effective sampling interval of the sub-region, $\Delta x_2$ can be defined by

$$\Delta x_2 = \Delta x_1 \frac{n}{m}, \tag{3.4}$$

where $\Delta x_1$ is the sampling interval of the hologram $m \times m$ and $n \times n$ and are the number of sub-region samples and total hologram samples, respectively. As shown in Fig. 3.6, if the light is propagated from the pixel of size $\Delta x_2$ to the plane distance of $z$, the size of the diffracted pixel will be defined by

$$\Delta x_3 = \frac{\lambda z}{\Delta x_2} \tag{3.5}$$

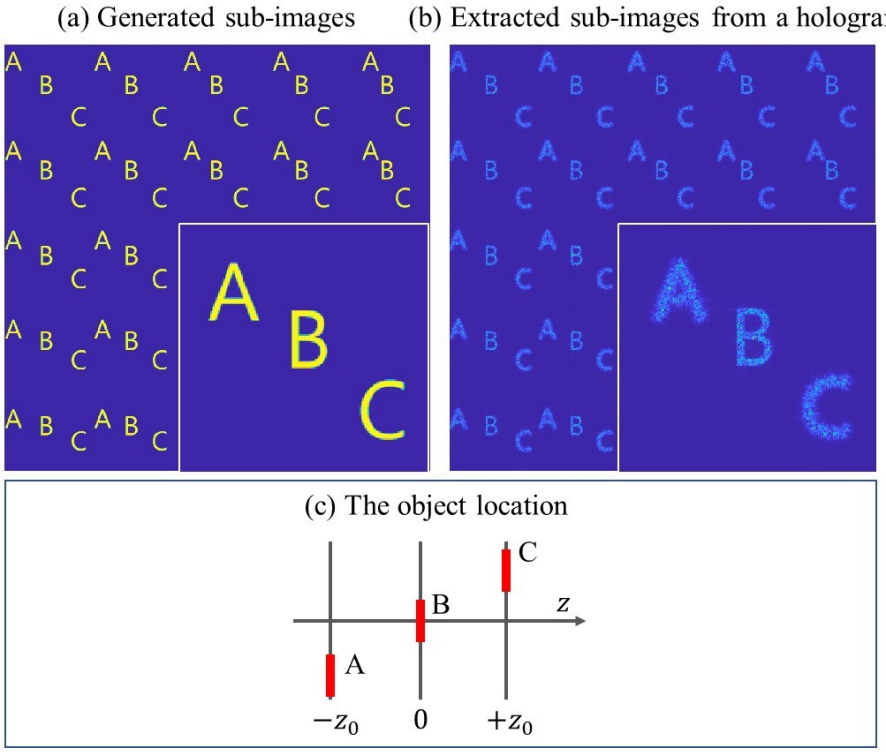


Figure 3.5 Comparison of generated sub-images by ray tracing (a) and extracted sub-images from a complex hologram. Blurs due to the out of focus and speckles due to the random phase cannot be observable in the generated sub-images.

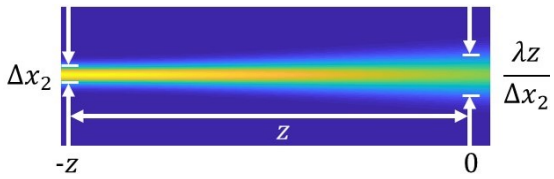


Figure 3.6 Beam diffraction condition for determining the size of the sub-region.

where $\lambda$ is the wavelength of light. The beam size ratio $R$ between the two planes is defined by

$$R = \frac{\lambda z}{\Delta x_2^2} = \frac{\lambda z}{\Delta x_1^2}\left(\frac{m}{n}\right)^2. \tag{3.6}$$

If $R$ is smaller than 1, the blur effect for a depth are relaxed. All-in-focus condition is satisfied if the condition,

$$\frac{\lambda z}{\Delta x_1^2} > \left(\frac{n}{m}\right)^2, \tag{3.7}$$

is satisfied. In Fig. 3.7, the extracted sub-images are compared with the generated ones when the Eq. (3.7) is satisfied. All sub-images are extracted from zero frequency. Wavelength is set to 532 nm, and the sampling interval of the hologram is $8\,\mu\mathrm{m}$. The total resolution of the hologram is $1026 \times 1026$. The $\Delta z$ is a distance to other depths. The letter 'A' is $\Delta z$ behind from 'B', and 'C' is $\Delta z$ before 'B'. Note that as the depth range of the object increases, the size of the sub-region should decrease, and the greater number of sub-regions are required.

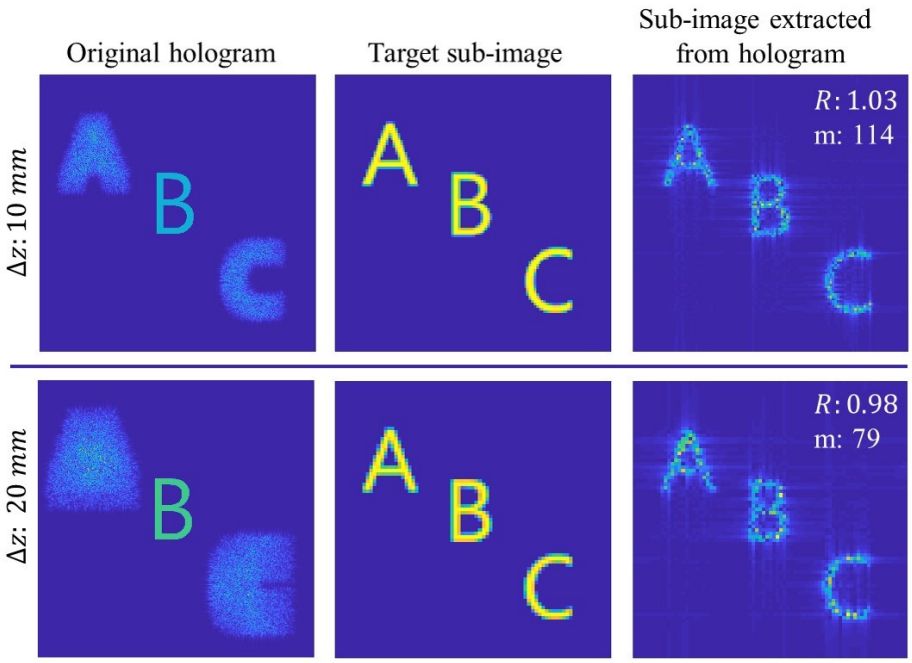


Figure 3.7 Comparison of the sub-images calculated by ray tracing method and extracted from real Fourier hologram, when the all-in-focus condition is met.

## 3.3 Optimization method and conditions

In the conventional Fourier ptychography, GS algorithm and iterative Fourier transform algorithm (IFTA) are used to solve the problem. As mentioned in the previous chapter, the convergence of these algorithms is influenced by the order in which sub-regions are processed. These computing order dependencies are even observable with the exact target images generated from the solution. The equations are reorganized by a single integrated least square problem to get rid of the order dependencies.

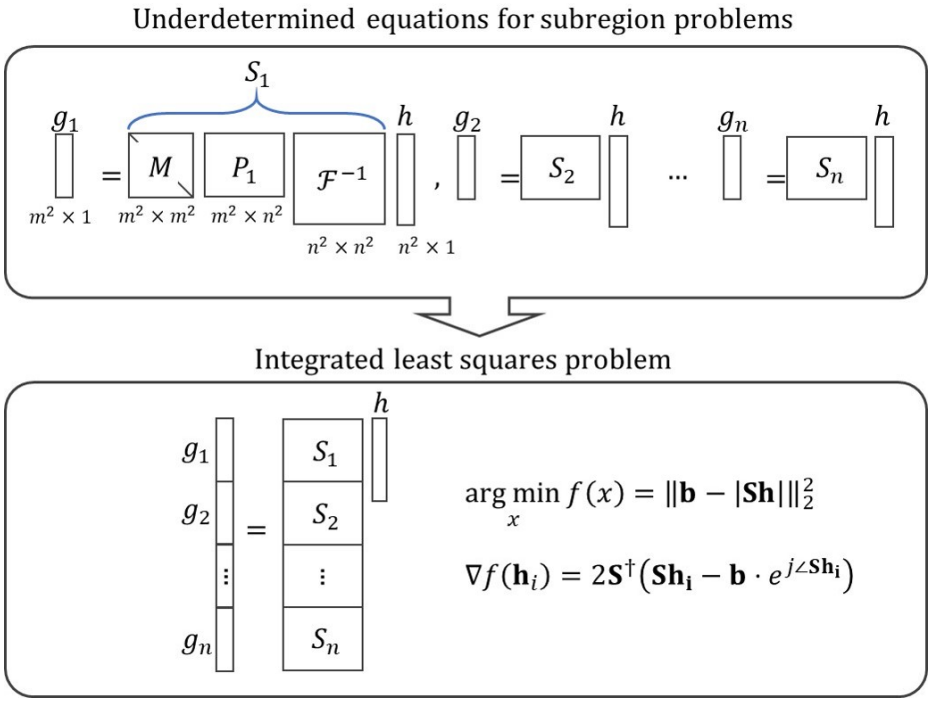


Figure 3.8 Matrix diagram of the integrated least squares problem.

As seen in Fig. 3.8, each small loop in sub-regions can be formulated under-determined equations with fat system matrices. In Fig. 3.8, $h$ is the hologram

to optimize, and $S_k$ are the system matrices to transform the local Fourier hologram into the sub-image for kth sub-region. The system matrix $S_k$ consists of the inverse Fourier transform matrix $\mathcal{F}^{-1}$, a projection matrix $P$, and a pupil mask $M$. The $g_n$ is the spatial profile of the nth sub-region. These $n$ equations share the hologram $h$, the unknown variable, so that all equations can be integrated in single equation. In the integrated equation, there is no order dependency because the gradient for each equation is processed all together at each iteration. The least squares problem is mathematically defined as

$$\arg\min_{\mathbf{h}} f(h) = \|\mathbf{b} - \mathbf{Sh}\|_2^2, \tag{3.8}$$

where, $\mathbf{b} \in \mathbb{R}^{n\times 1}$ is the target vector, $\mathbf{h} \in \mathbb{R}^{m\times 1}$ is unknown vectors to optimize, and $\mathbf{S} \in \mathbb{R}^{n\times m}$ is the system matrix. By the gradient descent (GD) algorithm, the gradient of $f(\mathbf{h}_i)$ at $i$th iteration can calculated by

$$\nabla f(\mathbf{h}_i) = 2\mathbf{S}^\dagger(\mathbf{Sh}_i - \mathbf{b}). \tag{3.9}$$

$\mathbf{h}_i$ can be updated by

$$\mathbf{h}_{i+1} = \mathbf{h}_i - \alpha \cdot \nabla f(\mathbf{h}_i). \tag{3.10}$$

The step size $\alpha$ is defined by

$$\alpha = \frac{\nabla f^\dagger(\mathbf{h}_i) \cdot \nabla f(\mathbf{h}_i)}{2\nabla f(\mathbf{h}_i)\mathbf{S}^\dagger\mathbf{S}\nabla f(\mathbf{h}_i)}. \tag{3.11}$$

In the Fourier ptychography, the problem is slightly different. First, all variables,

except the target image $\mathbf{b}$, are complex numbers, not real. Second, the target image value is amplitude-only. The phase profile in the spatial domain will remain as a degree of freedom. Therefore, the cost function is defined by

$$\arg\min_{\mathbf{h}} f(\mathbf{h}) = \|\mathbf{b} - |\mathbf{Sh}|\|_{\mathbf{2}}^{\mathbf{2}}. \tag{3.12}$$

the gradient of the cost function is calculated by

$$\nabla f(\mathbf{h}_i) = 2\left(\mathbf{S}^{\dagger}\left(\mathbf{Sh}_i - \mathbf{b}\cdot e^{j\angle \mathbf{Sh}_i}\right)\right). \tag{3.13}$$

While the system matrix $\mathbf{S}$ has a large dimension of $M^2 \times N^2$, the system matrix cannot be defined explicitly due to the lack of memories. All operation matrix $\mathbf{S}$ does is inverse Fourier transform, and the conjugate transpose of matrix $\mathbf{S}$, which is used to calculate the gradient, is also well defined by forward Fourier transform. Thus, it does not need to build a large scale matrix of $\mathbf{S}$ on memories. Only the output vector, after multiplied by matrix $\mathbf{S}$ is required to progress the computation. The pseudo code of the GD algorithm is described in Algorithm 3.1.

The comparison between the gradient method and the GS algorithm is represented in Fig. 3.9. For both algorithms, single point 1 mm in front of the hologram is used as an object. The total resolution of hologram is 204 $\times$ 204 pixels, the resolution of 37 $\times$ 37 sub-regions is 24 $\times$ 24 pixels. The sampling interval of the hologram is $8\,\mu\mathrm{m}$. The overlap ratio is 79%, and the beam size ratio is 1.15. The number of iterations 100 is used as stopping criteria. The target hologram is generated by the angular spectrum method. In the comparison, the GD algorithm shows better performance. The phase profile is well aligned, and the focal point is sharper than the GS algorithm. In the result of the GS al-

**Algorithm 3.1** Optimization process of Fourier ptychographic CGH

**Initialize:**

$i \leftarrow 0$

$\mathbf{h_o} \leftarrow$ initialized to random complex number

**repeat**

$$\nabla f(\mathbf{h}_i) \leftarrow 2\left(\mathbf{S}^{\dagger}\left(\mathbf{S}\mathbf{h}_i - \mathbf{b}\cdot e^{j\angle \mathbf{S}\mathbf{h}_i}\right)\right)$$
$$\alpha \leftarrow \frac{\nabla f^{\dagger}(\mathbf{h}_i)\cdot \nabla f(\mathbf{h}_i)}{2\nabla f(\mathbf{h}_i)\mathbf{S}^{\dagger}\mathbf{S}\nabla f(\mathbf{h}_i)}$$
$$\mathbf{h}_{i+1} \leftarrow \mathbf{h}_i - \alpha\cdot \nabla f(\mathbf{h}_i)$$

$i \leftarrow i+1$

**until** converge

gorithm, asymmetry of phase concentric circles is broken, and its spiral shapes follow the spiral order of sub-regions to update.

In the Fourier ptychography field, the embedded pupil function recovery (EPRY) is proposed to compensate for the aberration of the imaging system [87]. Inspired by the EPRY method, various masks are tested. Since there is no aberration in artificial sub-images, masks cannot be used to compensate for any aberrations. Instead, the mask filter can be utilized as an intermediate function to connect the artificial sub-images and the real solution of the hologram. As shown in Fig. 3.10, Gaussian filter shows excellent performance. Focusing ratio (FR) is the power ratio within the focal point for the total power of the images formulated by

$$FR = \frac{|u|^2_{max}}{\sum\limits_{x}|u|^2}, \tag{3.14}$$

where $u$ is an reconstructed complex field. The FR has a value close to 1 as the reconstructed hologram is closer to the ideal lens.

In the result of Fig. 3.10, although the beam size ratio is set to 2.35, the

performance is better than others. The convergence trend is also notable. The converged cost value is also significantly lower than others, and the convergence speed is also faster.

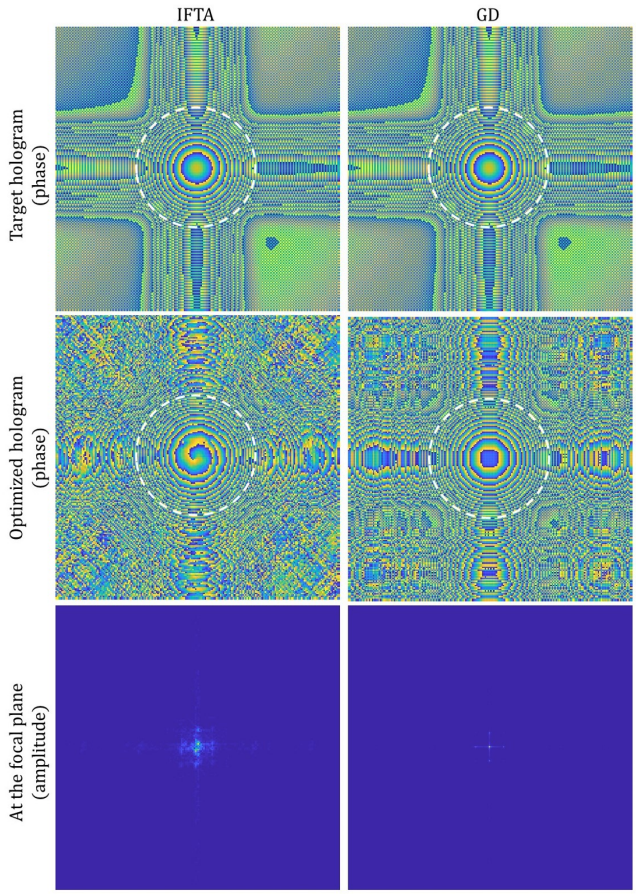


Figure 3.9 Numerical results of IFTA algorithm and GD algorithm. Due to the order dependency, the symmetry of the results break in IFTA algorithm.

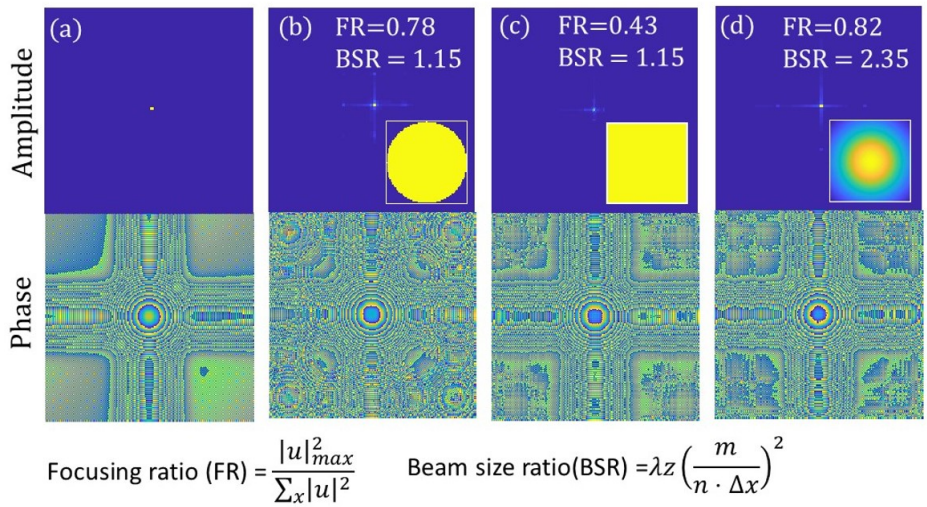


Figure 3.10 Comparison of generated hologram for the type of filter mask. (a) target phase profile and target amplitude on focus plane. (b) circular mask, (c) rectangular mask, and (d) Gaussian mask are applied for a pupil function.

## 3.4 Experimental results and analysis

A phase-only type liquid crystal on silicon (LCoS) display is used in the experiment, and $532\,\mathrm{nm}$ green laser diode is used as the light source. The SLM has a $4096 \times 2400$ of resolution and $3.74\times\ 3.74\,\mu\mathrm{m}$ pixel pitch. A Fourier CGH of $2400\times2400$ resolution is calculated by the proposed method. The depth range of the target 3D object is from $-2.5\,\mathrm{mm}$ to $2.8\,\mathrm{mm}$. The resolution of sub-region is set to $328 \times 328$, and the total number of the sub-region is set to $29 \times 29$. The overlapping region between adjacent sub-regions is set to $75\%$. To reconstruct the image, $2f$ system is used with $10\,\mathrm{cm}$ focal length. A DSLR camera with a macro lens is used to acquire the experimental results.

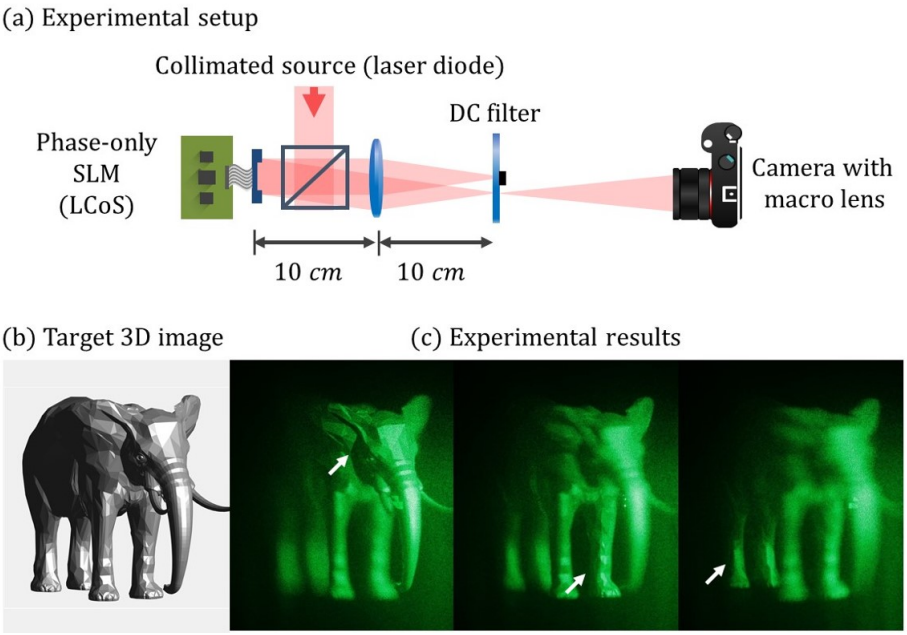


Figure 3.11 (a) Experimental setup, (b) target 3D object, and (c) reconstructed images with different focal depth.

Figure 3.11(c) shows that the focused region (white arrows) of the holo-

graphic image well represented as the focus plane is changed. The Fourier ptychographic CGH has another advantage over conventional IFTA. The IFTA is widely used to optimize CGHs into the phase-only hologram, but it is challenging to optimize the CGHs of 3D objects. Because the IFTA requires the target images at a particular depth plane perpendicular to the optical axis, the optimization is difficult unless the object images are well defined at certain planes. On the contrary, the target images of Fourier ptychography are well defined as sub-images on the local Fourier regions. The optimization for phase-only hologram can be easily implemented by adding the constraint that forces the solution to have phase-only values. The pseudo code is described in Algorithm 3.2.

**Algorithm 3.2** Optimization process for phase-only CGH

**Initialize:**

$i \leftarrow 0$

$\mathbf{h_o} \leftarrow$ initialized to random phase

**repeat**

$$\nabla f(\mathbf{h}_i) \leftarrow 2\left(\mathbf{S}^\dagger\left(\mathbf{S}\mathbf{h}_i - \mathbf{b}\cdot e^{j\angle \mathbf{S}\mathbf{h}_i}\right)\right)$$
$$\alpha \leftarrow \frac{\nabla f^\dagger(\mathbf{h}_i)\cdot\nabla f(\mathbf{h}_i)}{2\nabla f(\mathbf{h}_i)\mathbf{S}^\dagger\mathbf{S}\nabla f(\mathbf{h}_i)}$$
$$\mathbf{h}_{i+1} \leftarrow \exp\left\{j\angle\left(\mathbf{h}_i - \alpha\cdot\nabla f(\mathbf{h}_i)\right)\right\}$$
$$i \leftarrow i+1$$

**until** converge

In Fig. 3.12, the optimized hologram for phase-only SLM and the complex hologram, which of all amplitude values are flattened to 1 are compared experimentally and numerically. Although the DOF of the problem is not enough to show a clear difference in the experimental results, the background noise is noticeably reduced in the numerical results.

Figure 3.13 shows that the complexity of two algorithms, OLAS and Fourier ptychography. Two methods are shared a few common parameters. $m$ is the side

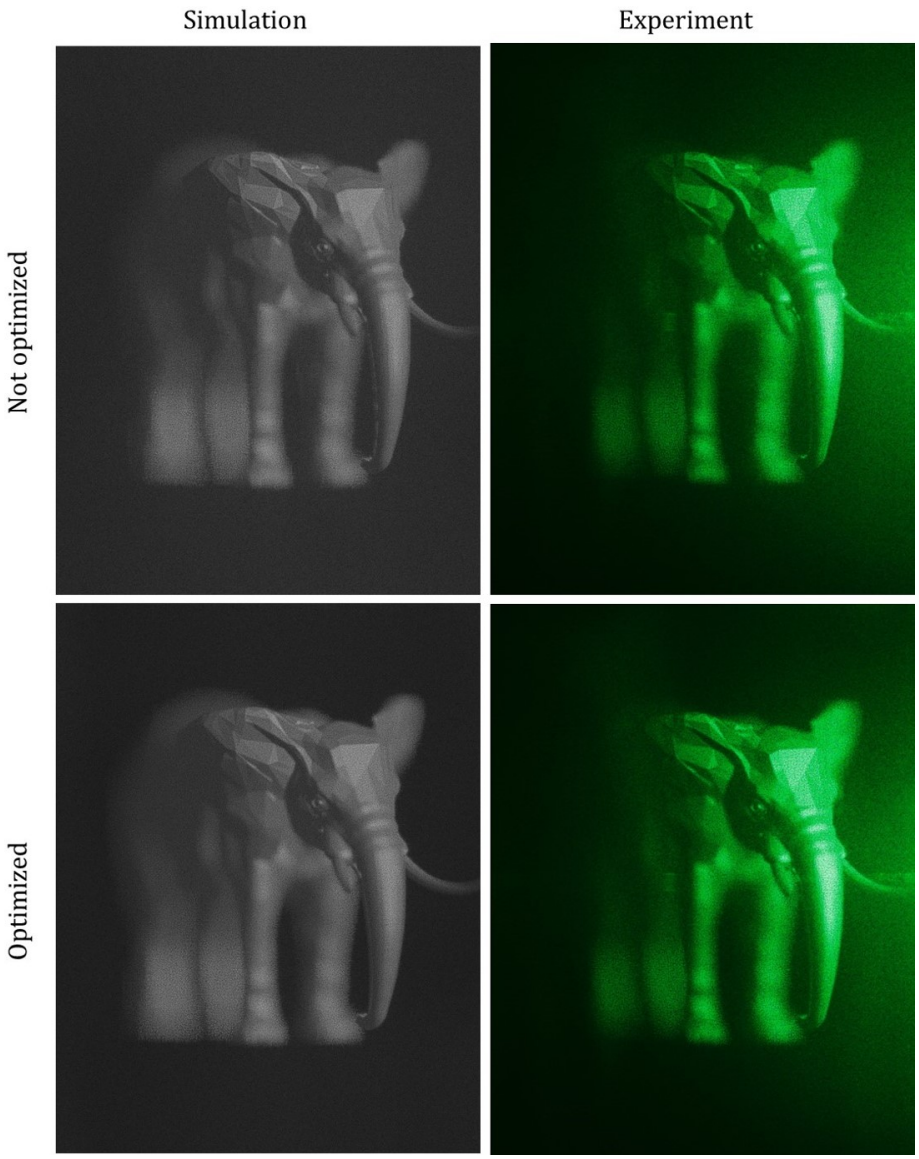


Figure 3.12 Experimental and numerical results of optimization for phase-only CGH.

length of the local regions for both algorithms, and $z$ is the maximum depth range of the target 3D objects. $z$ is defined by the distance from the origin. Depending on $z$ value, a suitable value of $m$ is varying in both methods, as shown in Fig. 3.13. $i$ is set to 20, and $r$ is set to 0.75 for the Fourier ptychographic method. The $\lambda$ is set to $532\,\mathrm{nm}$, $n$ is set to 2400, and $\Delta x$ is set to $3.74\,\mu\mathrm{m}$.

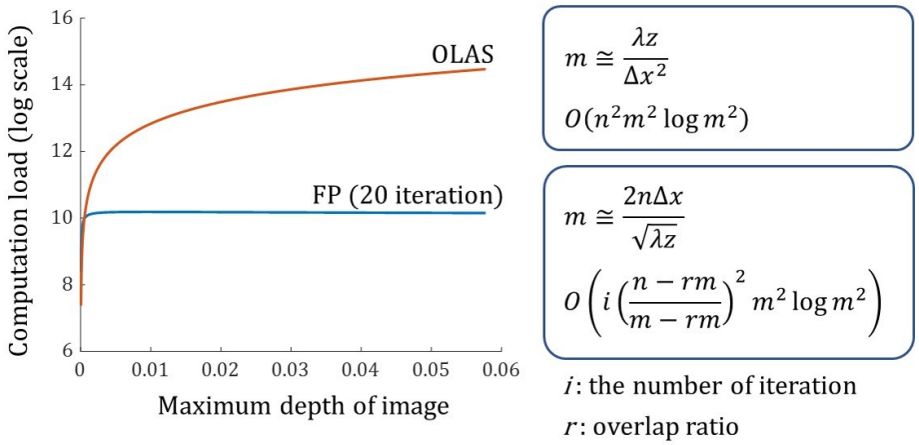


Figure 3.13 The complexity comparison of two algorithms, OLAS and Fourier ptychography for the depth range of target objects.

As shown in the graph of Fig. 3.13, Fourier ptychography has a much less computation load for the maximum depth range. Note that the y-axis of the graph is log scale. In the case of OLAS, the computation load increases proportionally as the maximum depth distance increases, while in the case of Fourier ptychography, there is an upper limit even if the depth range increases.

The image resolution is compared using point spread function (PSF) in Fig. 3.14. The quality of PSFs is measured by the focusing ratio defined in the previous session. CGHs are calculated by each method for a point $1.3\,\mathrm{cm}$ in front of holograms. The CGHs have $225 \times 255$ resolution, and the sampling interval

of CGHs is $6.4\,\mu\mathrm{m}$. The wavelength is set to $638\,\mathrm{nm}$.

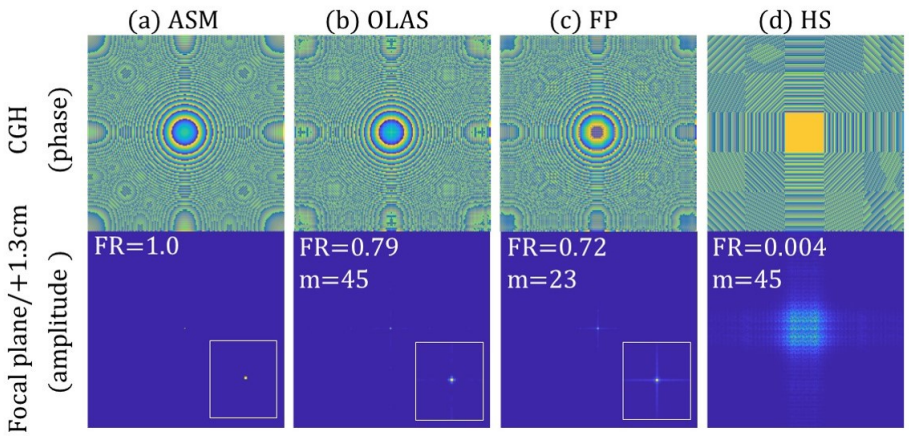


Figure 3.14 Comparison the focusing ratio of holograms calculated by (a) angular spectrum method, (b) overlap-add stereogram method, (c) Fourier ptychographic method, and (d) holographic stereogram method. Note that the phase and amplitude profile is from the different planes.

Fourier ptychography shows the moderate quality compared with the OLAS. In this case, the ptychographic method has 41.6% less computation load than the OLAS method. The computation load is calculated by the complexity equation in Fig. 3.13.

## 3.5 Conclusion

In this chapter, it is demonstrated that high-quality CGHs can be generated by the Fourier ptychographic method. Comparing to the other algorithms dealing with the light field, Fourier ptychographic CGH has advantages in resolution and computation. The comparison of algorithms can be found in Table 3.2.

Besides, Fourier ptychographic CGH does not require depth map data for sub-images. For synthesis data, the depth map is easy to generate, but for real scenes, it is not easy to extract precisely. Fourier ptychographic CGH also has the potential to be calculated in parallel. Fourier ptychographic CGH uses the gradient descent method, which is used widely in deep learning. In future work, calculation speed can be accelerated using general-purpose computing on the graphics processing unit (GPGPU).

Table 3.2 Algorithm comparison

| | **HS** | **OLAS** | **FP** | **Polygon** | **Point** |
|---|---|---|---|---|---|
| **Resolution** | low | high | high | high | high |
| **Computation** | low | high | medium | high | high |
| **Visual effects** | easy | easy | easy | hard | hard |

# Chapter 4. Noise reduction method for holographic multi-layered display

## 4.1 Introduction

A spatial light modulator (SLM) is the most crucial device for holographic displays. Liquid crystal displays (LCDs), liquid crystal on silicon (LCoS) [88], and digital micromirror devices (DMDs) [89] are the most widely used as a SLM for holographic displays. Since none of these SLMs are not fundamentally designed for holographic displays, these SLMs have some problems to use for holographic displays.

First, there is no commercial SLM that can modulate the amplitude and phase of light independently. LCD and LCoS can easily change between the two modulation types, amplitude and phase, using polarizers, but they cannot modulate both phase and amplitude of light simultaneously. Amplitude-only holograms produce twin noises that overlap with unwanted symmetrical images [20, 22, 23]. Twin noise can be eliminated with side-band filtering [20]. For amplitude-only holograms, the noises due to the modulation characteristic are mathematically well defined. The noise can be easily separated in Fourier domain. Complex holograms can be encoded to amplitude-only holograms utilizing side-band filtering [22]. In the case of phase-only holograms, noises are observable, but the noise is not well defined mathematically. Nevertheless, phase-only holograms can be encoded to complex holograms using side-band filtering [23]. Theoretically, both types of SLMs can modulate light in a complex manner, but the encoding methods cannot be used under some conditions in practice. For example, amplitude-only holograms with uneven energy distribu-

tion cannot encode appropriately in real-world SLMs because the encoded holograms require a deeper modulation depth than real SLMs provide. This is why complex type SLMs should be developed without mentioning the bulky optics required for the side filtering.

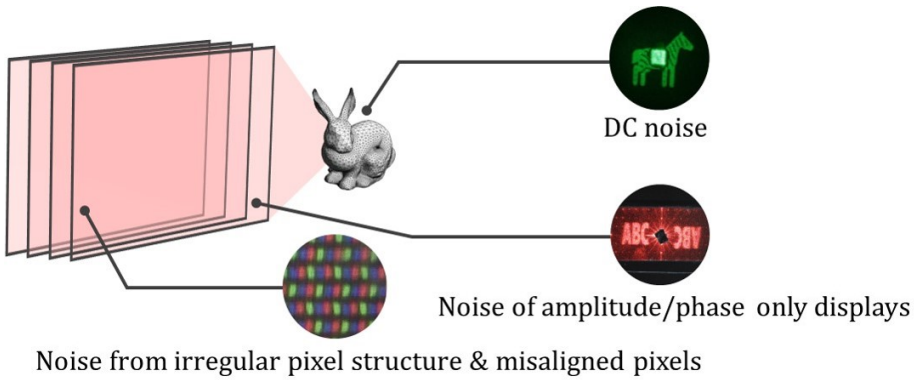


Figure 4.1 Inherent noises of the multi-layered holographic display

Secondly, regardless of the SLM type, the SLM has a discrete pixel structure. Due to the discrete pixel structure, high order images appear. There are studies to extend SBP utilizing these high order images [90, 91], but these high order images, which are noise in general conditions, have to be filtered in Fourier domain with additional optics. Furthermore, a fill factor of SLM causes non-uniform energy distribution on reconstructed images. The fill factor is the ratio of the light transmission area relative to the total pixel area. The lower fill factor is better for the uniform energy distribution, but the transmission efficiency will decrease. DC noise also arises with SLM with low fill factors. DC noise refers to transmitted light that has passed through an SLM but not modulated. The low fill factor means that the area of the black matrix that cannot modulate light is large.

Figure 4.1 shows the inherent noises of the multi-layered holographic dis-

plays. For practical holographic display, it is necessary to reduce these noises without an additional optical system. Fortunately, the multi-layered holographic display has a high degree of freedom as a computational display. In this chapter, the fundamental methods to reduce these noises by optimized CGHs are investigated.

## 4.2 Computer-generated hologram design method for DC noise elimination

### 4.2.1 Introduction

Noise management and filtering techniques are essential to the practical design of holographic display systems. It is well known that zero-order DC noise is generated due to a non-ideal finite fill-factor of less than 100%, and particularly strong DC noise can be harmful to an observer who is directly looking at the holographic display. The black matrix section of the SLM is the main cause of zero-order DC noise in a holographic display because the light field imposed on the black matrix becomes a totally uncontrollable component. For example, PLUTO (produced by HOLOEYE) has a fill factor of 87% and generates strong DC noise with 13% energy even when the phase value is accurately modulated as intended.

In Fig. 4.2, the origin of DC noise and related issues are presented using a simulation. In Fig. 4.2(a), a phase-only SLM with a 89% fill factor generates a diffraction image for a computer-generated hologram (CGH) in the image plane. The dark light field blocked by the black matrix pattern of a transmission-type SLM or the bright light field reflected by the black matrix pattern of a reflection-type SLM contributes to an uncontrollable DC noise pattern which is invariant to the dynamic modulation of the SLM pixels, as presented in Fig. 4.2(b). In Fig. 4.2(c), the DC pattern and its periodic replication appear at the center of the diffraction image and in the higher order domain, respectively. In general, to avoid DC noise, the off-axis method is used [22], in which the linear grating phase profile is multiplied by the CGH to shift the signal to the off-axis first order diffraction domain and a DC rejection filter masks the zero-order noise formed in the zero-order diffraction domain [92]. This off-axis holographic dis-

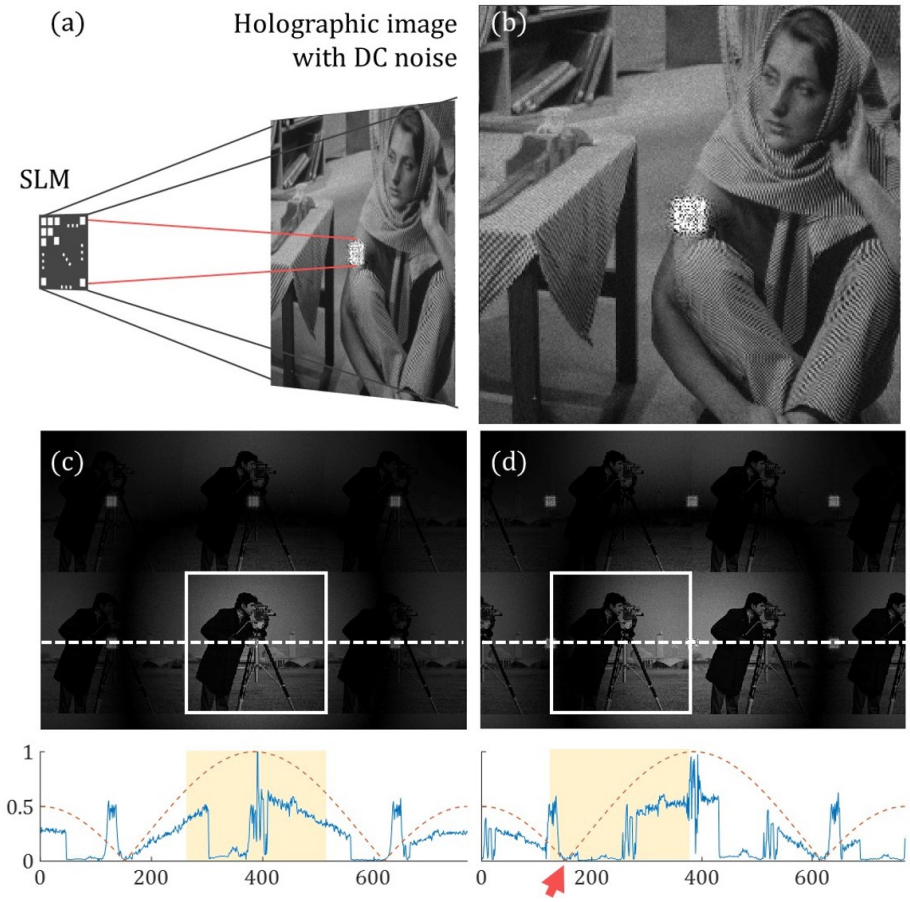


Figure 4.2 (a) Conventional Fresnel holographic display setup and (b) the diffraction image with DC noise using the conventional setup. High order intensity distribution with DC noise of a conventional holographic display: (c) on-axis mode and its cross-sectional profile (blue line) with the sinc envelope (dotted orange line), and (d) off-axis mode and its cross-sectional profile with the sinc envelope. Note that the peaks in the blue line represent DC noise.

play setup is widely used for DC noise suppression in holographic displays; in practice, however, it suffers from a technical limitation related to the finite pixel size. In Figs. 4.2(c) and 4.2(d), high order diffraction images with DC noise appearing on the holographic display in on-axis and off-axis mode are compared, respectively. Because SLM pixels are rectangular, the diffraction image is modulated by a sinc function envelope profile across the higher order diffraction domain. The problem is that the sinc function contains two-dimensional zero nodal lines as shown in Figs. 4.2(c) and 4.2(d). The lower panels of Figs. 4.2(c) and 4.2(d) present the cross-sectional profile of the on-axis and off-axis modes. The on-axis display creates a diffraction image in the main lobe region (the yellow region), while the off-axis mode places the image across the zero node (the red arrow) to avoid DC noise interfering with the diffraction image. The practical obstacle for on-axis holographic displays is the overlap of uncontrollable DC noise and the diffraction image in the zeroth-order domain, while the limitation for the off-axis display mode is the intensity modulation by the sinc-envelope profile. Near the zero nodal lines, the sinc profile modulates the diffraction image to be significantly darker; this loss of energy is thought to be an inherent defect of off-axis holographic display mode that is difficult to eliminate with an SLM that has rectangular pixels.

### 4.2.2 Optical system and two-step iterative Fourier transform algorithm

In this dissertation, A DC-noise free on-axis for multi-layered holographic display and essential algorithm for the optimal synthesis of CGHs for this configuration are proposed. In Fourier optics, optical information noise filters typically take the form of an optical Fourier transform-based configuration. For example, the 4-f system-based single-side band holographic display system is conve-

nient [22], but its multiple lenses render it bulky, meaning it cannot be applied in a more compact system configuration. In order to reduce the zero-order DC noise in an on-axis configuration using a single phase SLM, we need to devise a new type of optical filter and new optimal design algorithm for phase hologram patterns. Figure 4.3 illustrates a schematic of the proposed system and the CGH synthesis algorithm. A spherically converging wave generated using a convex lens is incident on the SLM and the DC component is focused to a point in the focal filtering plane, which can be considered a Fourier plane. Although this setup has an advantage in that it makes the system more compact compared to the conventional off-axis holographic display configuration, a significant structural issue remains in that the DC rejection filter may interfere with the signal diffraction field of the CGH, generating a shadow (i.e., a dark field) on the image plane. In order to solve this problem, we modify the CGH to render the shadow of the DC rejection filter invisible at the image plane and form a designed diffraction image. In order to realize this scenario, we propose a two-step iterative Fourier transform algorithm (IFTA), illustrated in Fig. 4.3. This algorithm is an extended version of the conventional IFTA, which considers the forward wave propagation from the CGH plane to the image plane passing through the rejection filter plane and the direct backward propagation from the image plane to the CGH plane without interference by the filter. The transforms of the forward and backward propagations are referred to as the sequential Fresnel transform (SFrT) and the inverse Fresnel transform (iFrT), respectively.

The system is composed of two sections: (1) from the CGH plane ($\vec{r}_1$ plane) to the DC-rejection filter plane ($\vec{r}_2$ plane), and (2) from the filter plane to the image plane ($\vec{r}_3$ plane). The distance from the CGH plane to the filter plane and that from the filter plane to the image plane are denoted by $d_1$ and $d_2$, respectively. The spherical wave incident on the SLM is represented by $l(\vec{r}_1)$ and the

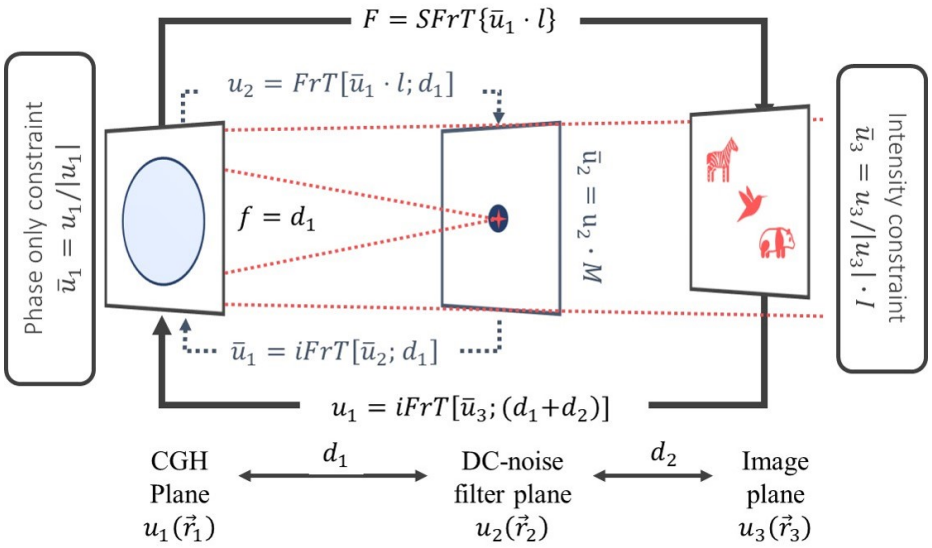


Figure 4.3 The schematic of the proposed DC-noise free holographic display system and two-step IFTA for CGH synthesis. The lens behind the SLM represents the spherical backlight carrier wave. Note that the calculation for the small blue loop is already included in the SFrT function, so the large black loop represents the entire calculation process

CGH pattern $u_1(\vec{r}_1)$ modulates $l(\vec{r}_1)$ to $u_1(\vec{r}_1) \cdot l(\vec{r}_1)$ so that the DC noise is focused at the focal point of the incident spherical wave $l(\vec{r}_1)$, where the DC noise can be effectively filtered by a rejection filter of minimum diameter (Fig. 4.3). In most situations, $d_1$ is set to $f$, the focal length of the incident spherical wave $l(\vec{r}_1)$. On the filter plane, the center of the light field is blocked by the binary filter mask, denoted by $m(\vec{r}_2)$, while the light field passing through the outside of the filter mask continues to propagate to the image plane and form the diffraction image $u_3(\vec{r}_3)$. The Fresnel transform, $FrT\{f(\vec{r}_1; z\}$, is defined by

$$FrT\left\{f(\vec{r}_1); z\right\} = \frac{-j}{|\lambda z|} \int_{-\infty}^{+\infty} f(\vec{r}_1) \exp\left\{\frac{j\pi}{\lambda z}(\vec{r}_2 - \vec{r}_1)^2\right\} d\vec{r}_1. \tag{4.1}$$

In this system configuration, the diffraction field, $u_3(\vec{r}_3)$ can be calculated using the cascade of the conventional Fresnel transform:

$$u_3(\vec{r}_3) = FrT\left\{FrT\left\{u_1(\vec{r}_1) \cdot l(\vec{r}_1); d_1\right\} \cdot m(\vec{r}_2); d_2\right\}, \tag{4.2}$$

However, in this case, a numerical problem occurs with respect to the sampling schemes on the image plane. Note that the impulse response form of the Fresnel transform is used instead of the transfer function form. Let the sampling intervals of the CGH plane be $\Delta\vec{r}_1$. For Eq. (4.2), the sampling interval on the image plane $\Delta\vec{r}_3$ will be $\Delta\vec{r}_1 d_2/d_1$. Let us consider the situation when the DC-noise filter disappears in space. A single Fresnel transform from the CGH plane to the image plane is described by

$$u_3(\vec{r}_3) = FrT\left\{u_1(\vec{r}_1); d_1 + d_2\right\}. \tag{4.3}$$

In this case, the sampling interval on the image plane $\Delta\vec{r}_3$ is $\lambda(d_1+d_2)/N\Delta\vec{r}_1$, where $N$ is the number of samples. The sampling schemes for Eq. (4.2) and Eq. (4.3) contradict each other since the sampling interval $\Delta\vec{r}_1$ is proportional to $\Delta\vec{r}_3$ according to Eq. (4.2), while this relationship is reciprocally proportional in Eq. (4.3). The discretization processing of the two integral transforms, Eq. (4.2) and Eq. (4.3), thus reveals a mismatch in the sampling scheme. To avoid this problem, the following wave propagation process is adopted. First, optical waves are propagated from the CGH plane to the filter plane; the optical field obscured by the DC-noise mask function $m(\vec{r}_2)$is

$$\bar{u}_2(\vec{r}_2) = m(\vec{r}_2) FrT\left\{u_1(\vec{r}_1)\cdot l(\vec{r}_1); d_1\right\}. \tag{4.4}$$

Instead of transferring $\bar{u}_2(\vec{r}_1)$ to the image plane directly, we use a two-step propagation algorithm. The first step is the inverse Fresnel transform (iFrT) of $\bar{u}_2(\vec{r}_1)$ to the CGH plane, and the second is the forward Fresnel transform of the optical field to the image plane. This two-step propagation is represented by

$$u_3(\vec{r}_3) = FrT\left\{iFrT\left\{\bar{u}_2(\overrightarrow{r_2}); d_1\right\}; d_1+d_2\right\}. \tag{4.5}$$

The forward propagation of the entire system can be summarized as the sequential Fresnel transform (SFrT) defined by

$$\begin{aligned} u_3 &= SFrT\left\{u_1\cdot l\right\} \\ &= FrT\left\{iFrT\left\{FrT\left\{u_1\cdot l; d_1\right\}\cdot m; d_1\right\}; d_1+d_2\right\}. \end{aligned} \tag{4.6}$$

The back-propagation from the image plane to the CGH plane can be written using the inverse Fresnel transform:

$$u_1(\vec{r}_1) = iFrT\left\{u_3(\vec{r}_3); d_1 + d_2\right\}. \tag{4.7}$$

Now, the IFTA can be constructed using SFrT and iFrT. The resulting flow chart for the proposed IFTA is depicted in Fig. 4.3. The primary objective of the IFTA is to find a phase-only CGH in the input CGH plane so that the intensity conditions at the image plane are satisfied simultaneously [93,94]. The proposed two-step IFTA can relax the sampling condition of Fresnel transform. If the spacing between optical layers is narrow, Fresnel transform cannot be used due to sampling condition, but the sampling condition can be satisfied using the proposed method. In the proposed IFTA scheme, the filter plane is subject to an additional constraint in that the shadow of the DC-rejection filter should be invisible at the image plane in order to form a designed diffraction image.

### 4.2.3 Numerical and experimental results

In Figs. 4.4(a) and 4.4(b), the numerically reconstructed holographic images of CGHs optimized using the two-step IFTA with and without the DC-rejection filter are compared. The diffraction image without the DC-rejection filter exhibits significant deterioration due to the DC around the center of the image plane (Fig. 4.4a), while the DC noise has been clearly removed from the diffraction with the use of the 2.4 mm $\times$ 2.4 mm rectangular DC-rejection filter (Fig. 4.4b). There is a limit to the size of the DC-rejection filter, but this can be compensated for in the proposed system. This means that if the size of the DC-rejection filter goes past its maximum width, a dark shadow cast by the DC-rejection filter begins to appear around the center of the image plane, spreading gradually in the radial direction, with the dark shadow pattern reflecting the diffraction pattern of the shape of the DC-rejection filter (Fig. 4.4c). For a single point at the center of

the image plane of the proposed system, the maximum size of the DC-rejection filter is determined geometrically as shown in Fig. 4.4(d). If the DC-rejection filter blocks the entire light path at one point on the image plane, this cannot be resolved, even with the proposed IFTA method. It is thus important to design a system so that some part of the light from the CGH plane is delivered to the center region of the output plane without interference by the filter. To achieve this, the maximum diffraction angle, $\theta_{max}$ is given by $\lambda/\Delta x_3$ at the image plane under paraxial approximation. The maximum width of the DC-blocking filter $D_{max}$ can then be determined as

$$D_{\max} = d_2\theta_{max} = N\Delta x_1 d_2/(d_1 + d_2), \tag{4.8}$$

where $N$ is the number of sampling points on one side. Fig. 4.4(e) presents the change in the mean squared error (MSE) for the CGH image by DC-rejection filter width, and the trends supports Eq. (4.8). In the analysis, the pixel pitch of the SLM, $\Delta x_1$, is set to $8\,\mu\mathrm{m}$, and $d_1$ and $d_2$ are set to 0.4 m and 0.6 m, respectively. When $N$ is set to 256 and 512, the maximum width of the filter is estimated to be about 1.23 mm and 2.46 mm, respectively.

In order to validate the proposed system and algorithm, we conducted a holographic display experiment. The proposed system was represented by a simple experimental set up consisting of a He-Ne laser (632 nm), a phase-only SLM (PLUTO of HoloEye Inc.) with a $1920 \times 1080$ resolution, an $8\,\mu\mathrm{m}$ pixel pitch and a fill-factor of 87%, and conventional 2-inch optical components (Fig. 4.5a). The optical length and are 25 cm and 55 cm respectively, and the radius of the DC-filter is 3 mm. The DC filter is made of round black paper on glass substrate. The first step in the experiment was the optical reconstruction and observation of diffraction images with and without DC noise through a field lens

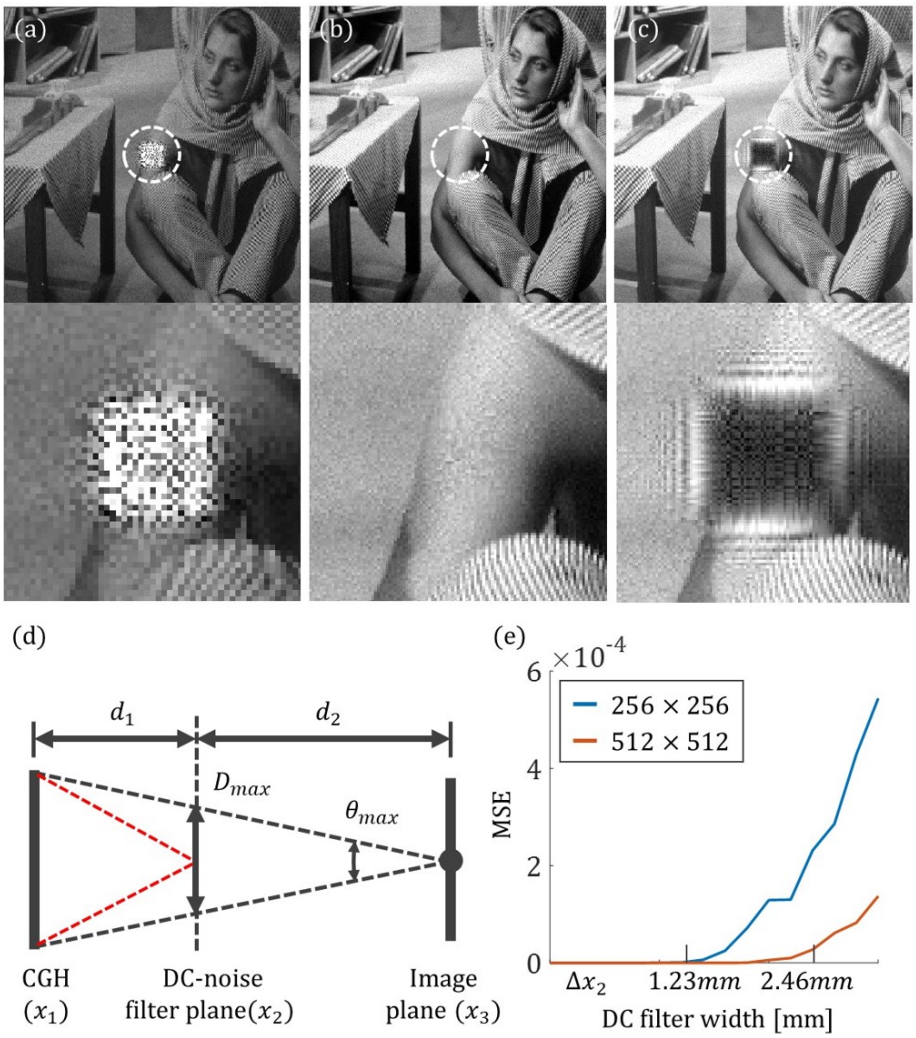


Figure 4.4 Numerical results of the DC-noise filtering simulation. Diffraction image calculated using the IFTA (a) without a DC-rejection filter and (b) with a 2.4 mm wide DC-rejection filter. (c) The appearance of the shadow of the DC-rejection filter, the size of which (5 mm) is larger than the maximum filter size. (d) The geometrical consideration of the maximum DC-rejection filter size. (e) The relationship between MSE and DC-rejection filter width.

to demonstrate the free holographic 3D display at the single image plane. The experimental results are presented in Figs. 4.5(b) and 4.5(c) for clear comparison. The holographic images were taken with a commercial DSLR camera. As previously seen in Fig. 4.2, a diffraction image affected by DC-noise is observed in Fig. 4.5(b). However, the DC-noise can be removed in the same experimental setup by using the DC-rejection filter and the CGH calculated by the proposed method as shown in Fig. 4.5(c).

In Fig. 4.6, the proposed technique for a DC-noise-free on-axis holographic 3D display is demonstrated by presenting multi-level depth-map CGH images from both numerical simulations and experiments. For this experiment, the two-step IFTA technique to extend the conventional multi-level depth map CGH synthesis algorithm is used [92]. The application of the two-step IFTA to multi-level 3D CGH image synthesis is straightforward. The multi-level CGH can be obtained by alternately computing the iterative loops for each depth image. Figures 4.6(a)- 4.6(d) present observation photos of the holographic 3D images generated by the on-axis holographic display configuration demonstrating a clear 4-depth level accommodation effect. At each depth, the corresponding part of the holographic image comes into focus and the other parts are blurred due to the out-of-focus effect. Although this setup has an on-axis configuration, the DC-noise of the phase-only PLUTO SLM was successfully removed and does not affect the resulting holographic 3D image, thus the DC-rejection filter is invisible to the viewer. These experimental results are further supported by the simulation results in the right column. The left panels of Figs. 4.6(a) and 4.6(d) focused on the words ‘KOREA’ and ‘LAB’ separated by 125 cm along the optic axis. Consequently, the proposed holographic display system can successfully express multiple planes focused at different depths with no DC noise. In conclusion, A DC-free on-axis holographic display scheme using a phase-only SLM

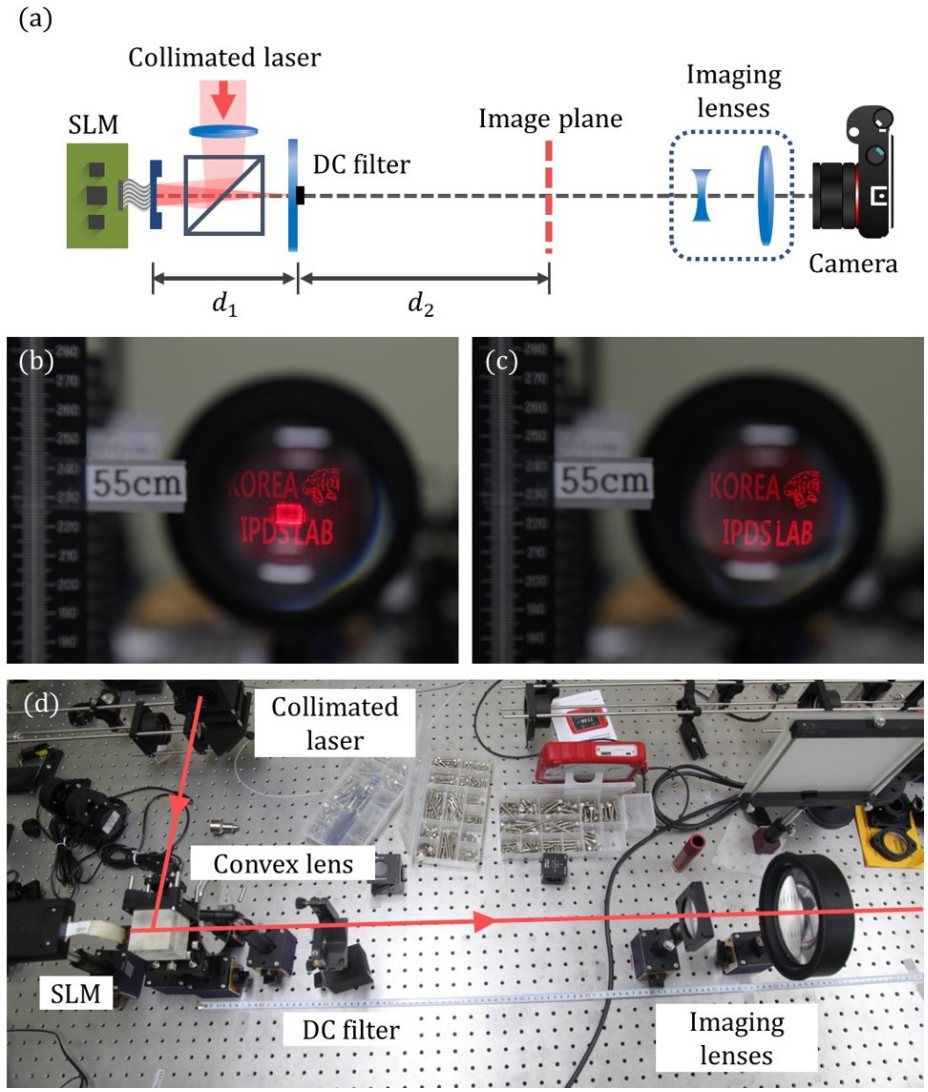


Figure 4.5 (a) Schematic diagram of the experimental setup for the holographic 3D display. Experimental results for the filtering DC-noise simulation. (b) The conventional IFTA without a DC-rejection filter. (c) The proposed IFTA with a DC-rejection filter. (d) Experimental setup.

without DC-noise has been proposed. For this, a two-step iterative Fourier transform algorithm with a DC-rejection filter was devised. The proposed technique can be applied not only to multi-layered holographic display but also general holographic 3D display configurations such as holographic lithography, holographic trapping, and tweezers, which typically require high energy efficiency.

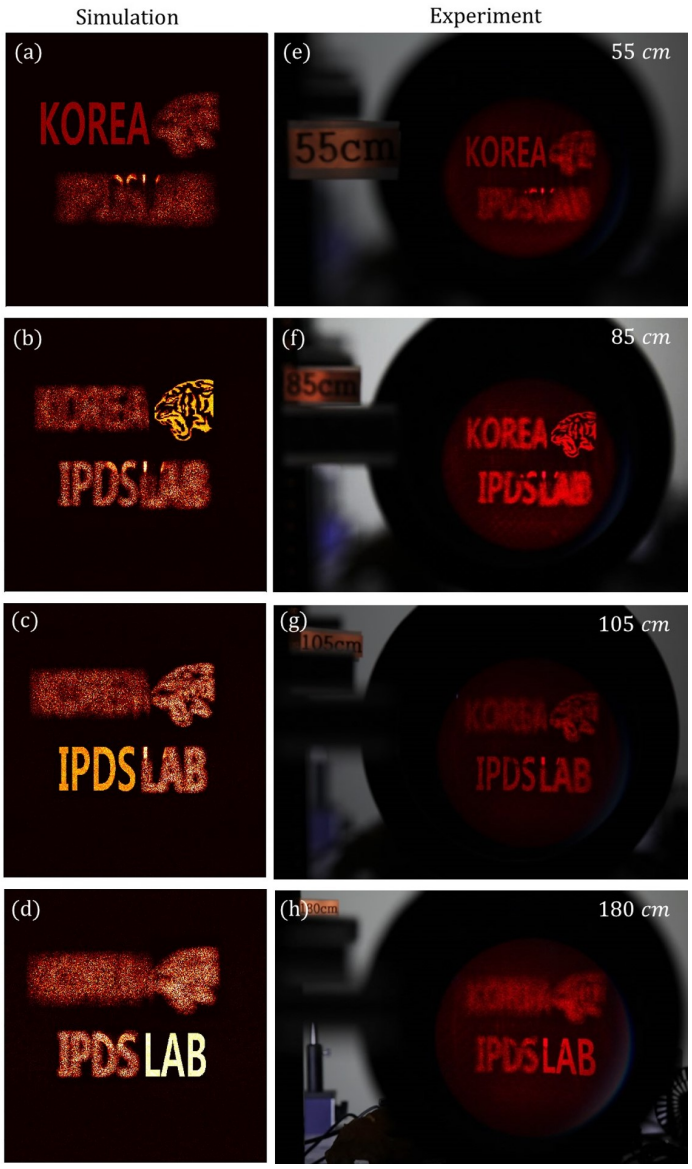


Figure 4.6 The holographic images of the numerical results with focus at (a) 55 cm, (b) 85 cm, (c) 105 cm, and (d) 180 cm, and the matched experimental results with focus at (e) 55 cm, (f) 85 cm, (g) 105 cm, and (h) 180 cm.

## 4.3 Computer-generated hologram for multi-layered holographic displays with irregular pixel structure

### 4.3.1 introduction

With the development of high-resolution, high-density displays for mobile devices, various pixel arrangements have been studied to use subpixels effectively [95, 96]. For example, PenTile is the method to arrange subpixels for achieving high-resolution display with fewer subpixels. As a result, the subpixel structure is not uniformly allocated. As shown in Fig. 4.7, not like the traditional RGB structure, the other structures have a zigzag subpixel structure for each channel.

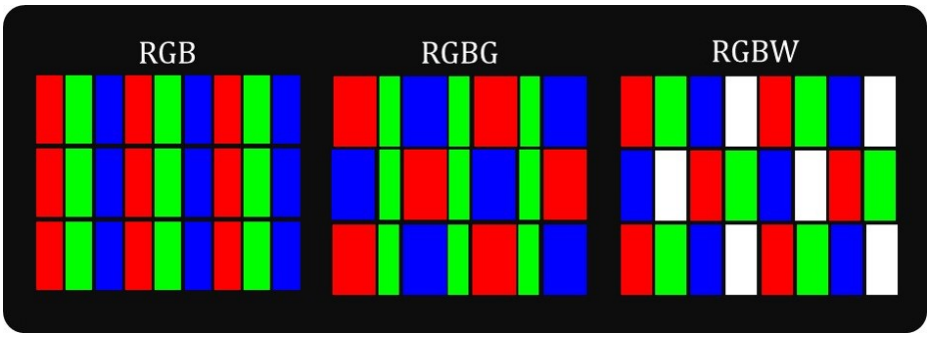


Figure 4.7 The example of various pixel structure

Since the space-bandwidth product (SBP) is proportional to the number of pixels, the holographic displays require a display panel with high resolution and high pixel density. The conventional methods to generate CGHs are supposed to use a uniform and orthogonal computation grid. Thus, the generated CGH will cause aliasing in the reconstructed images. For example, in the case of RGBW, in Fig. 4.7, if only the odd or even lines are used, the pixel structure is uniform and orthogonal. Display with irregular pixel structures can be decomposed by a

few sets of regular pixel structures. Inspired by this fact, the CGH design method to compensate irregular pixel structures is proposed.

### 4.3.2 Compensation of computer-generated hologram for multi-layered holographic displays with irregular pixel structure

In typical spatial light modulators (SLMs), the pixels are orthogonally and uniformly arranged. While the displays techniques utilizing pixel structure arise, the commercial LCDs with high pixel density often have an irregular pixel structure. In the case of PenTile structure, there are two types of PenTile, RGBG, and RGBW. Both types have a zigzag pixel structure, as shown in Fig. 4.7. Odd and even rows are misaligned. Algorithms for computing computer-generated hologram (CGH) are mostly based on uniform grids, so it is not easy to calculate CGH for these irregular SLMs. If the CGH calculated for uniform grids is used as it is, noise occurs, as shown in Fig. 4.9. The pixel structure should be decomposed into a superposition of regular structures. For example, suppose the pixel alignment is misaligned, line by line, to the vertical direction, as shown in Fig. 4.9(b). In this case, when pixels are decomposed into a set of odd and even rows, each pixel structure is orthogonal. The odd set and even set are shifted by a certain distance from each other, and this shift can be expressed by the Fourier shift theorem,

$$\mathcal{F}\left\{h(x-\Delta_x, y-\Delta_y)\right\} = H(f_x, f_y)\exp\left\{-j2\pi\left(\Delta_x f_x + \Delta_y f_y\right)\right\}, \quad (4.9)$$

where $f_x$ and $f_y$ are spatial frequency of the Fourier domain, and $\Delta_x$ and $\Delta_y$ are disparity in x and y-axis, respectively. This means that the shifted pixels can be compensated by multiplying the exponential term in Fourier domain. In Fig. 4.8, workflow of the proposed algorithm is represented.

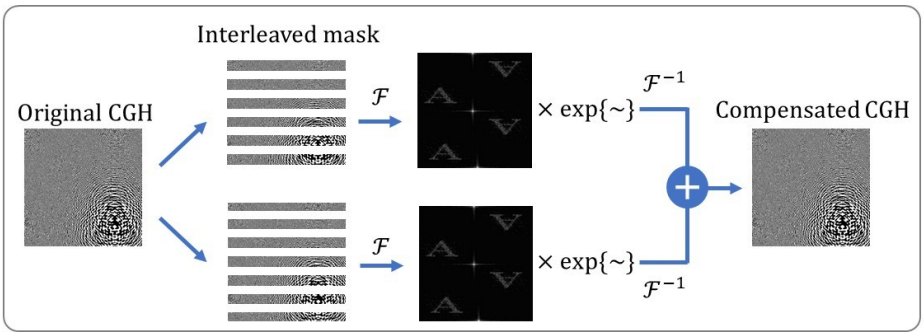


Figure 4.8 Workflow of the compensation algorithm.

In Fig. 4.8, the workflow to compensate misaligned pixels is described. In this example, suppose that the odd and even lines are well aligned in their lines. Note that the CGH is expected to compensate for the misalignment, and the CGH is still calculated based on the orthogonal grid, and the original CGH is a Fourier hologram. The original CGH is decomposed into two interleaved fields. Since each field is sampled twice roughly in the vertical direction, Fourier transform of these fields causes aliasing to the vertical direction. After multiplying the exponential term of Eq. (4.9), two fields are superposed again. Finally, the CGH is calculated for compensating a specific pixel structure. In this example, the original CGH is decomposed into only two fields but can be decomposed into multiple fields depending on the pixel. In Fig. 4.9, the numerical results are represented. Suppose that the SLM is amplitude-only type, and a single sideband holography method [22] is used to encoding complex signals to amplitude-only signal. Without compensation, the ghost images appear, as shown in Fig. 4.9(b).

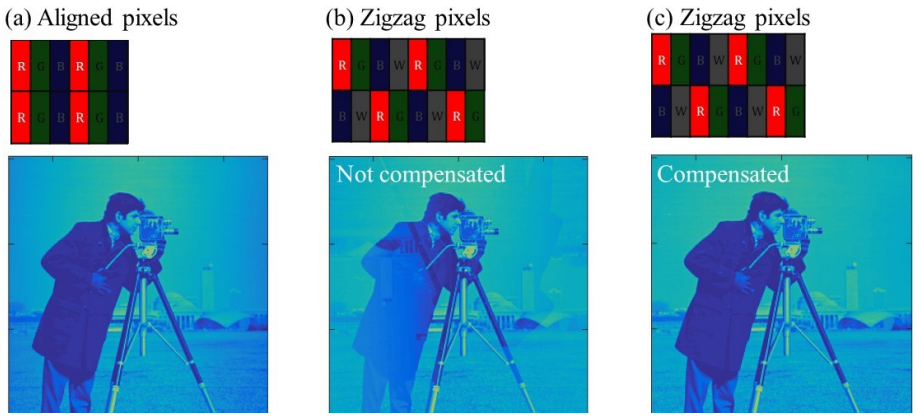


Figure 4.9 Numerically reconstructed holographic images by SLMs of (a) uniformly aligned pixel structure, and (b,c) zigzag pixel structure. Note that (b) the ghost images are appeared in the case of the zigzag structure, and (c) the ghost images are clearly reduced by the proposed alogrithm.

### 4.3.3 Experimental results

In Fig. 4.10, the experiment configuration is represented. Three RGB lasers with $457\,\mathrm{nm}$, $532\,\mathrm{nm}$, and $660\,\mathrm{nm}$ are used for coherent light source. All lasers are spatially filtered and collimated and combined by the beam splitters. A continuous neutral density (ND) filter is used to control the power of lasers.

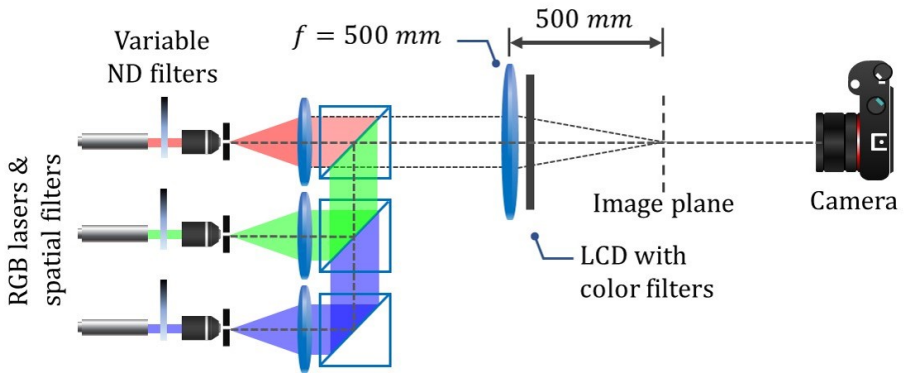


Figure 4.10 The schematic diagram of the experimental setup

The RGB LCD panel with RG/BR/GB sub-pixel structure, as shown in Fig. 4.11(c) is used as amplitude-only SLM. Note that the resolution of SLM is specified to 3840 $\times$ 2160, but the real number of the pixel for each color channel is 3840 $\times$ 1440. Achromatic doublet lens with a 500 mm focal length is used for reconstruction of Fourier hologram. The DSLR camera acquires the experimental results with a 1:1 macro lens. The pixel pitches of the SLM are $45.8\,\mu\mathrm{m}$ and $30.5\,\mu\mathrm{m}$ for horizontal and vertical directions, respectively.

Figure 4.11(a) shows that the unwanted ghost images (white arrows) appear without compensation. Using compensated CGH, the noises are disappeared in Fig. 4.11(b). Note that the noises are barely observable in the experiment for the green and blue channels. The noise is clearly observable only in the red channel because the disparity between odd and even rows of the red channel is $30.53\,\mu\mathrm{m}$,

three-times longer than other channels.

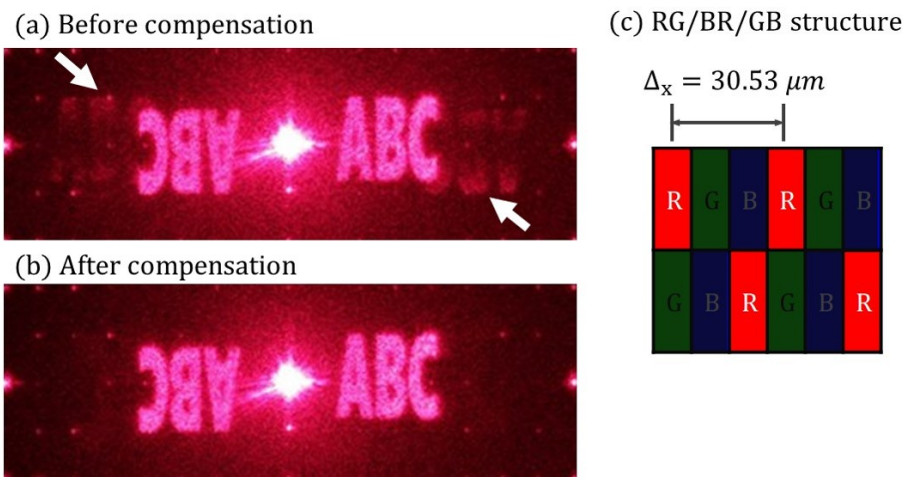


Figure 4.11 Experimental results for a red channel only: reconstructed image (a) without compensation and (b) with compensation. (c) Schematic diagram of RG/BR/GB pixel structure.

Figure 4.12 shows the experimental result for all RGB channels. RGB channels are digitally combined after measured separately. All three images for each channel are measured under the exact same condition. The only translation is applied for the alignment. Thanks to the achromatic lens, focal length for each wavelength is the same, but in Fourier hologram, the sampling interval at the image plane is determined by

$$\Delta x_2 = \frac{\lambda z}{T_x}, \tag{4.10}$$

where the $T_x$ is the side length of the SLM. The sampling interval is proportional to $\lambda$. Thus the target image size should be resized. In this experiment, the images for each wavelength are resized based on a blue wavelength. Resizing ratios are

$457/660$, $457/532$, and $457/457$ for each RGB channel. As seen in Fig. 4.12, the size of images is well matched.

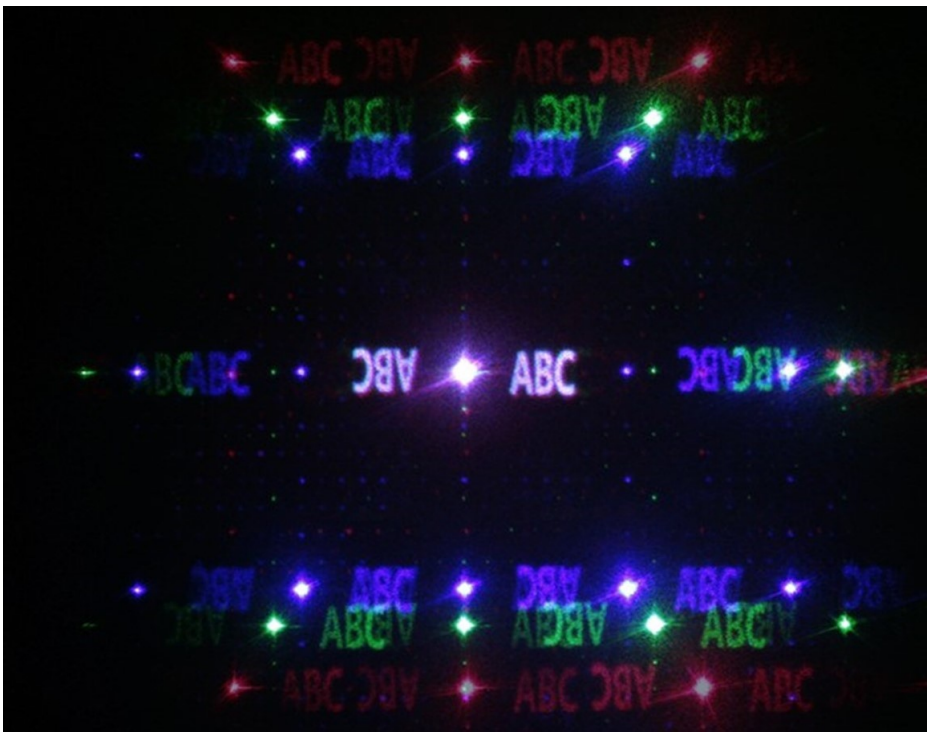


Figure 4.12 Experimental result for RGB channels.

## 4.4 Conclusion

In this chapter, the method to reduce the inherent noises of holographic displays is proposed and investigated. DC noise is the harshest noise for holographic displays and requires the bulky 4-f system to filter the noise. The 4f system is not only bulky but also causes various aberrations unless precisely designed optics are used. The off-axis scheme to separate the DC noise from the signal also has a problem with the zero nodes of the sinc energy envelope. A two-step IFTA with a DC-rejection filter was devised to solve a problem. A two-step IFTA has an advantage in avoiding sampling problems. According to the propagation depth and the size of the computation grid, usage of the Fresnel method and angular spectrum (AS) method can be often subtle, but the proposed two-step IFTA is applicable to the case that the sampling condition of Fresnel transform cannot meet. The proposed technique also can be applied to general holographic 3D display configurations such as large-aperture and wide-viewing angle multiple SLM array configurations, holographic lithography, holographic trapping, and tweezers, which typically require high energy efficiency. The CGH compensation method for the display, which has an irregular sub-pixel structure, is also introduced. The proposed method can be generalized for any displays with an arbitrary structure of sub-pixels. This technique can be used to compensate misaligned pixels and can be used to compensate misaligned displays of the multi-layered holographic displays. For practical multi-layered holographic displays, the inherent noises of the display should be eliminated. In future work, these noise reduction methods could be implied to the CGH optimization process.

# Chapter 5. Conclusion

Holographic displays are the ultimate 3D display that can reconstruct images at high resolution while satisfying all 3D cues. The development of display panels with high pixel density and resolution is essential for practical holographic displays. The resolution of a display panel is gradually increasing, but the pixel density is physically limited to increase. The SBP of the holographic display is proportional to the number of pixels. However, given the form factor of the system and the additional optics required, high pixel density is essential to realizing a practical holographic display.

In this dissertation, the novel architecture of computational multi-layered holographic display is proposed to overcome the limitation of conventional 2D displays. In the proposed method, by stacking the pixels along the third dimension, the effective pixel density of a display system can be increased. While the synthesis of CGH for the layered displays is not straightforward, the layered displays have a high degree of freedom (DOF). This means that the layered displays as a computational display have the potential to play various roles using this DOF.

The CGH generation method for the layered display to extend the SBP is proposed, and it is shown that SBP of the display can be extended with the properly optimized CGH. On the other hand, it is also demonstrated that the complex modulation can be achieved with multiple phase-only or amplitude-only SLMs. Depending on how the CGH is optimized, the resource proportional to the number of pixels can be flexibly shared with various factors such as SBP, modulation type, and others.

Since the conventional CGH generation methods have a trade-off between

the computation load and the quality of reconstructed images, they are not suitable for extremely high-resolution displays such as the multi-layered display. Thus, the efficient CGH synthesis method via Fourier ptychography is proposed and investigated. The proposed method has the advantages of both the light-field based methods and Fresnel based methods. The computation load is relatively moderate for other methods. The image quality is as good as the Fresnel methods because it does not approximate wave to the bundle of rays. The proposed method also can easily generate CGHs of real scenes because it uses light-field data, which is easy to obtain by light-field cameras.

Reducing the inherent noises of displays is also a significant issue for practical holographic displays, and these inherent noises are also problematic for the multi-layered display. The methods to reduce inherent noises from the display panels are investigated. DC noise is the most effective noise to degrade image quality. The compact layered optics system and CGH design method for the system are proposed to eliminate the DC noise. It is demonstrated that the proposed method can eliminate the DC noise, avoiding the loss of energy due to the sinc envelope. This method shows that the holographic information can be designed to pass through certain obstacles such as DC filters and form the image.

CGH design method for compensating the noise from the irregular sub-pixel structure is proposed. The commercialized LCDs with high-density pixels often have an irregular sub-pixel structure, and it causes severe ghost images on the holographic images. This technique can be applied to any sub-pixel structure, and it is expected to compensate for the noise due to the pixel alignment of the multi-layered holographic displays.

In Fig. 5.1, the proposed methods in this dissertation are described. Multi-layered holographic display architecture is proposed for exploiting the conventional low-resolution displays, and elemental technologies for building the prac-

tical holographic display are proposed.

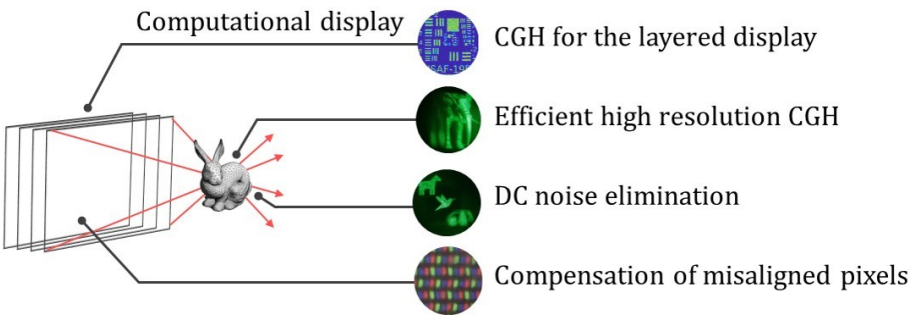


Figure 5.1 The proposed methods for the multi-layered holographic display.

For future work, two approaches are recommended. First, the multi-layered holographic display has great potential with high DOF to implement all the proposed techniques. For example, the DC noise filtering technique is also applicable to the layered display because each layer can be operated with a lens and DC filter. If an integrated optimization method is developed, it will be a big step to the practical holographic that can control noises and SBP.

Secondly, the previous research shows that optical multi-layers can operate certain linear operations and contain specific information [63]. Since the 3D objects often have overlapped information for their viewing angles, and natural images also have common features, the information of images can be compressed. By learning the common information of images to the static optical layers, it can be expected to extend the SBP of single SLM.

# Bibliography


[1] P. Milgram, H. Takemura, A. Utsumi, and F. Kishino, "Augmented reality: A class of displays on the reality-virtuality continuum," in *Telemanipulator and telepresence technologies*, vol. 2351, pp. 282–292, International Society for Optics and Photonics, 1995.

[2] M. A. Livingston, W. F. Garrett, G. Hirota, M. C. Whitton, E. D. Pisano, H. Fuchs, *et al.*, "Technologies for augmented reality systems: realizing ultrasound-guided needle biopsies," in *Proceedings of the 23rd annual conference on computer graphics and interactive techniques*, pp. 439–446, ACM, 1996.

[3] R. T. Azuma, "A survey of augmented reality," *Presence: Teleoperators & Virtual Environments*, vol. 6, no. 4, pp. 355–385, 1997.

[4] H. Kaufmann and D. Schmalstieg, "Mathematics and geometry education with collaborative augmented reality," in *ACM SIGGRAPH 2002 conference abstracts and applications*, pp. 37–41, ACM, 2002.

[5] S. J. Watt, K. Akeley, M. O. Ernst, and M. S. Banks, "Focus cues affect perceived depth," *Journal of vision*, vol. 5, no. 10, pp. 7–7, 2005.

[6] M. Lambooij, M. Fortuin, I. Heynderickx, and W. IJsselsteijn, "Visual discomfort and visual fatigue of stereoscopic displays: A review," *Journal of Imaging Science and Technology*, vol. 53, no. 3, pp. 30201–1–30201–14, 2009.

[7] B. Lee, "Three-dimensional displays, past and present," *Phys. Today*, vol. 66, no. 4, pp. 36–41, 2013.

[8] D. Lanman and D. Luebke, "Near-eye light field displays," *ACM Transactions on Graphics (TOG)*, vol. 32, no. 6, p. 220, 2013.

[9] W. Song, Y. Wang, D. Cheng, and Y. Liu, "Light field head-mounted display with correct focus cue using micro structure array," *Chinese Optics Letters*, vol. 12, no. 6, p. 060010, 2014.

[10] A. Maimone, G. Wetzstein, M. Hirsch, D. Lanman, R. Raskar, and H. Fuchs, "Focus 3d: Compressive accommodation display," *ACM Transactions on Graphics (TOG)*, vol. 32, no. 5, p. 153, 2013.

[11] F.-C. Huang, G. Wetzstein, B. A. Barsky, and R. Raskar, "Eyeglasses-free display: towards correcting visual aberrations with computational light field displays," *ACM Transactions on Graphics (TOG)*, vol. 33, no. 4, p. 59, 2014.

[12] C. Jang, K. Bang, S. Moon, J. Kim, S. Lee, and B. Lee, "Retinal 3d: augmented reality near-eye display via pupil-tracked light field projection on retina," *ACM Transactions on Graphics (TOG)*, vol. 36, no. 6, p. 190, 2017.

[13] S. Lee, Y. Jo, D. Yoo, J. Cho, D. Lee, and B. Lee, "Tomographic near-eye displays," *Nature communications*, vol. 10, no. 1, p. 2497, 2019.

[14] A. Mermillod-Blondin, E. McLeod, and C. B. Arnold, "High-speed varifocal imaging with a tunable acoustic gradient index of refraction lens," *Optics letters*, vol. 33, no. 18, pp. 2146–2148, 2008.

[15] G. D. Love, D. M. Hoffman, P. J. Hands, J. Gao, A. K. Kirby, and M. S. Banks, "High-speed switchable lens enables the development of a volumetric stereoscopic display," *Optics express*, vol. 17, no. 18, pp. 15716–15725, 2009.

[16] C.-K. Lee, S. Moon, S. Lee, D. Yoo, J.-Y. Hong, and B. Lee, "Compact three-dimensional head-mounted display system with savart plate," *Optics express*, vol. 24, no. 17, pp. 19531–19544, 2016.

[17] D. Smalley, E. Nygaard, K. Squire, J. Van Wagoner, J. Rasmussen, S. Gneiting, K. Qaderi, J. Goodsell, W. Rogers, M. Lindsey, *et al.*, "A photophoretic-trap volumetric display," *Nature*, vol. 553, no. 7689, p. 486, 2018.

[18] R. Hirayama, D. M. Plasencia, N. Masuda, and S. Subramanian, "A volumetric display for visual, tactile and audio presentation using acoustic trapping," *Nature*, vol. 575, no. 7782, pp. 320–323, 2019.

[19] D. L. Fried, "Laser eye safety: the implications of ordinary speckle statistics and of speckled-speckle statistics," *JOSA*, vol. 71, no. 7, pp. 914–916, 1981.

[20] O. Bryngdahl and A. Lohmann, "Single-sideband holography," *JOSA*, vol. 58, no. 5, pp. 620–624, 1968.

[21] H. Song, G. Sung, S. Choi, K. Won, H.-S. Lee, and H. Kim, "Optimal synthesis of double-phase computer generated holograms using a phase-only spatial light modulator with grating filter," *Optics express*, vol. 20, no. 28, pp. 29844–29853, 2012.

[22] H. Kim, C.-Y. Hwang, K.-S. Kim, J. Roh, W. Moon, S. Kim, B.-R. Lee, S. Oh, and J. Hahn, "Anamorphic optical transformation of an amplitude spatial light modulator to a complex spatial light modulator with square pixels," *Applied optics*, vol. 53, no. 27, pp. G139–G146, 2014.

[23] C. Hsueh and A. Sawchuk, "Computer-generated double-phase holograms," *Applied optics*, vol. 17, no. 24, pp. 3874–3883, 1978.

[24] V. Arrizón, G. Méndez, and D. Sánchez-de La-Llave, "Accurate encoding of arbitrary complex fields with amplitude-only liquid crystal spatial light modulators," *Optics Express*, vol. 13, no. 20, pp. 7913–7927, 2005.

[25] C. Burckhardt, "A simplification of lee's method of generating holograms by computer," *Applied optics*, vol. 9, no. 8, pp. 1949–1949, 1970.

[26] B. R. Brown and A. W. Lohmann, "Complex spatial filtering with binary masks," *Applied optics*, vol. 5, no. 6, pp. 967–969, 1966.

[27] S. Reichelt, R. Häussler, G. Fütterer, N. Leister, H. Kato, N. Usukura, and Y. Kanbayashi, "Full-range, complex spatial light modulator for real-time holography," *Optics letters*, vol. 37, no. 11, pp. 1955–1957, 2012.

[28] D. A. Gregory, J. C. Kirsch, and E. C. Tam, "Full complex modulation using liquid-crystal televisions," *Applied optics*, vol. 31, no. 2, pp. 163–165, 1992.

[29] G.-Y. Lee, G. Yoon, S.-Y. Lee, H. Yun, J. Cho, K. Lee, H. Kim, J. Rho, and B. Lee, "Complete amplitude and phase control of light using broadband holographic metasurfaces," *Nanoscale*, vol. 10, no. 9, pp. 4237–4245, 2018.

[30] E.-Y. Song, J. Cho, H. Kim, W. Y. Choi, and B. Lee, "Double bi-material cantilever structures for complex surface plasmon modulation," *Optics express*, vol. 23, no. 5, pp. 5500–5507, 2015.

[31] Y. Mori, T. Fukuoka, and T. Nomura, "Speckle reduction in holographic projection by random pixel separation with time multiplexing," *Applied optics*, vol. 53, no. 35, pp. 8182–8188, 2014.

[32] Y. Takaki and M. Yokouchi, "Speckle-free and grayscale hologram reconstruction using time-multiplexing technique," *Optics express*, vol. 19, no. 8, pp. 7567–7579, 2011.

[33] S. Kubota and J. W. Goodman, "Very efficient speckle contrast reduction realized by moving diffuser device," *Applied optics*, vol. 49, no. 23, pp. 4385–4391, 2010.

[34] Y. Kuratomi, K. Sekiya, H. Satoh, T. Tomiyama, T. Kawakami, B. Katagiri, Y. Suzuki, and T. Uchida, "Speckle reduction mechanism in laser rear projection displays using a small moving diffuser," *JOSA A*, vol. 27, no. 8, pp. 1812–1817, 2010.

[35] X. Chen, Ø. Svensen, M. N. Akram, *et al.*, "Speckle reduction in laser projection using a dynamic deformable mirror," *Optics express*, vol. 22, no. 9, pp. 11152–11166, 2014.

[36] L. Wang, T. Tschudi, T. Halldorsson, and P. R. Petursson, "Speckle reduction in laser projection systems by diffractive optical elements," *Applied optics*, vol. 37, no. 10, pp. 1770–1775, 1998.

[37] J. Pauwels and G. Verschaffelt, "Speckle reduction in laser projection using microlens-array screens," *Optics express*, vol. 25, no. 4, pp. 3180–3195, 2017.

[38] D. Li, D. P. Kelly, and J. T. Sheridan, "Speckle suppression by doubly scattering systems," *Applied optics*, vol. 52, no. 35, pp. 8617–8626, 2013.

[39] J.-W. Pan and C.-H. Shih, "Speckle reduction and maintaining contrast in a laser pico-projector using a vibrating symmetric diffuser," *Optics express*, vol. 22, no. 6, pp. 6464–6477, 2014.

[40] M. N. Akram, Z. Tong, G. Ouyang, X. Chen, and V. Kartashov, "Laser speckle reduction due to spatial and angular diversity introduced by fast scanning micromirror," *Applied optics*, vol. 49, no. 17, pp. 3297–3304, 2010.

[41] A. Lapchuk, G. Pashkevich, O. Prygun, I. Kosyak, M. Fu, Z. Le, and A. Kryuchyn, "Very efficient speckle suppression in the entire visible range by one two-sided diffractive optical element," *Applied Optics*, vol. 56, no. 5, pp. 1481–1488, 2017.

[42] D. Lee, C. Jang, K. Bang, S. Moon, G. Li, and B. Lee, "Speckle reduction for holographic display using optical path difference and random phase generator," *IEEE Transactions on Industrial Informatics*, vol. 15, no. 11, pp. 6170–6178, 2019.

[43] A. W. Lohmann, R. G. Dorsch, D. Mendlovic, Z. Zalevsky, and C. Ferreira, "Space–bandwidth product of optical signals and systems," *JOSA A*, vol. 13, no. 3, pp. 470–473, 1996.

[44] Y. Takaki and K. Fujii, "Viewing-zone scanning holographic display using a mems spatial light modulator," *Optics express*, vol. 22, no. 20, pp. 24713–24721, 2014.

[45] Y. Takaki and M. Nakaoka, "Scalable screen-size enlargement by multi-channel viewing-zone scanning holography," *Optics express*, vol. 24, no. 16, pp. 18772–18781, 2016.

[46] T. Inoue and Y. Takaki, "Table screen 360-degree holographic display using circular viewing-zone scanning," *Optics express*, vol. 23, no. 5, pp. 6533–6542, 2015.

[47] Y. Sando, D. Barada, and T. Yatagai, "Holographic 3d display observable for multiple simultaneous viewers from all horizontal directions by using a time division method," *Optics letters*, vol. 39, no. 19, pp. 5555–5557, 2014.

[48] Z. M. A. Lum, X. Liang, Y. Pan, R. Zheng, and X. Xu, "Increasing pixel count of holograms for three-dimensional holographic display by optical scan-tiling," *Optical Engineering*, vol. 52, no. 1, p. 015802, 2013.

[49] Y. Takaki and N. Okada, "Reduction of image blurring of horizontally scanning holographic display," *Optics express*, vol. 18, no. 11, pp. 11327–11334, 2010.

[50] K. Yamamoto, Y. Ichihashi, T. Senoh, R. Oi, and T. Kurita, "3d objects enlargement technique using an optical system and multiple slms for electronic holography," *Optics express*, vol. 20, no. 19, pp. 21137–21144, 2012.

[51] Y. Takaki, M. Yokouchi, and N. Okada, "Improvement of grayscale representation of the horizontally scanning holographic display," *Optics express*, vol. 18, no. 24, pp. 24926–24936, 2010.

[52] Y.-Z. Liu, X.-N. Pang, S. Jiang, and J.-W. Dong, "Viewing-angle enlargement in holographic augmented reality using time division and spatial tiling," *Optics express*, vol. 21, no. 10, pp. 12068–12076, 2013.

[53] Y. Lim, K. Hong, H. Kim, H.-E. Kim, E.-Y. Chang, S. Lee, T. Kim, J. Nam, H.-G. Choo, J. Kim, *et al.*, "360-degree tabletop electronic holographic display," *Optics express*, vol. 24, no. 22, pp. 24999–25009, 2016.

[54] J. Hahn, H. Kim, Y. Lim, G. Park, and B. Lee, "Wide viewing angle dynamic holographic stereogram with a curved array of spatial light modulators," *Optics express*, vol. 16, no. 16, pp. 12372–12386, 2008.

[55] H. Sasaki, K. Yamamoto, K. Wakunami, Y. Ichihashi, R. Oi, and T. Senoh, "Large size three-dimensional video by electronic holography using multiple spatial light modulators," *Scientific reports*, vol. 4, p. 6177, 2014.

[56] H. Yu, K. Lee, J. Park, and Y. Park, "Ultrahigh-definition dynamic 3d holographic display by active control of volume speckle fields," *Nature Photonics*, vol. 11, no. 3, p. 186, 2017.

[57] J. Park, K. Lee, and Y. Park, "Ultrathin wide-angle large-area digital 3d holographic display using a non-periodic photon sieve," *Nature communications*, vol. 10, no. 1, p. 1304, 2019.

[58] D. Lanman, M. Hirsch, Y. Kim, and R. Raskar, "Content-adaptive parallax barriers: optimizing dual-layer 3d displays using low-rank light field factorization," *ACM Transactions on Graphics (TOG)*, vol. 29, no. 64, p. 163, 2010.

[59] G. Wetzstein, D. Lanman, M. Hirsch, and R. Raskar, "Tensor displays: compressive light field synthesis using multilayer displays with directional backlighting," *ACM Transactions on Graphics (TOG)*, vol. 31, no. 4, pp. 1–11, 2012.

[60] S. Lee, C. Jang, S. Moon, J. Cho, and B. Lee, "Additive light field displays: realization of augmented reality with holographic optical elements," *ACM Transactions on Graphics (TOG)*, vol. 35, no. 4, p. 60, 2016.

[61] T. D. Gerke and R. Piestun, "Aperiodic volume optics," *Nature photonics*, vol. 4, no. 3, p. 188, 2010.

[62] J. Chang, V. Sitzmann, X. Dun, W. Heidrich, and G. Wetzstein, "Hybrid optical-electronic convolutional neural networks with optimized diffractive optics for image classification," *Scientific Reports*, vol. 8, no. 1, p. 12324, 2018.

[63] X. Lin, Y. Rivenson, N. T. Yardimci, M. Veli, Y. Luo, M. Jarrahi, and A. Ozcan, "All-optical machine learning using diffractive deep neural networks," *Science*, vol. 361, no. 6406, pp. 1004–1008, 2018.

[64] J. W. Goodman, *Introduction to Fourier optics*. Roberts and Company Publishers, 2005.

[65] D. G. Voelz, *Computational fourier optics: a MATLAB tutorial*. SPIE press Bellingham, WA, 2011.

[66] M. Hirsch, G. Wetzstein, and R. Raskar, "A compressive light field projection system," *ACM Transactions on Graphics (TOG)*, vol. 33, no. 4, p. 58, 2014.

[67] A. Cauchy, "Méthode générale pour la résolution des systemes d'équations simultanées," *Comp. Rend. Sci. Paris*, vol. 25, no. 1847, pp. 536–538, 1847.

[68] M. E. Lucente, "Interactive computation of holograms using a look-up table," *Journal of Electronic Imaging*, vol. 2, no. 1, pp. 28–35, 1993.

[69] S.-C. Kim and E.-S. Kim, "Effective generation of digital holograms of three-dimensional objects using a novel look-up table method," *Applied Optics*, vol. 47, no. 19, pp. D55–D62, 2008.

[70] T. Shimobaba, H. Nakayama, N. Masuda, and T. Ito, "Rapid calculation algorithm of fresnel computer-generated-hologram using look-up table and

wavefront-recording plane methods for three-dimensional display," *Optics Express*, vol. 18, no. 19, pp. 19504–19509, 2010.

[71] J. Weng, T. Shimobaba, N. Okada, H. Nakayama, M. Oikawa, N. Masuda, and T. Ito, "Generation of real-time large computer generated hologram using wavefront recording method," *Optics Express*, vol. 20, no. 4, pp. 4018–4023, 2012.

[72] D. Arai, T. Shimobaba, K. Murano, Y. Endo, R. Hirayama, D. Hiyama, T. Kakue, and T. Ito, "Acceleration of computer-generated holograms using tilted wavefront recording plane method," *Optics express*, vol. 23, no. 2, pp. 1740–1747, 2015.

[73] H. Kim, J. Hahn, and B. Lee, "Mathematical modeling of triangle-mesh-modeled three-dimensional surface objects for digital holography," *Applied optics*, vol. 47, no. 19, pp. D117–D127, 2008.

[74] K. Matsushima and S. Nakahara, "Extremely high-definition full-parallax computer-generated hologram created by the polygon-based method," *Applied optics*, vol. 48, no. 34, pp. H54–H63, 2009.

[75] H. Nishi, K. Matsushima, and S. Nakahara, "Rendering of specular surfaces in polygon-based computer-generated holograms," *Applied optics*, vol. 50, no. 34, pp. H245–H252, 2011.

[76] Y. Zhao, L. Cao, H. Zhang, D. Kong, and G. Jin, "Accurate calculation of computer-generated holograms using angular-spectrum layer-oriented method," *Optics express*, vol. 23, no. 20, pp. 25440–25449, 2015.

[77] J.-S. Chen, D. Chu, and Q. Y. Smithwick, "Rapid hologram generation utilizing layer-based approach and graphic rendering for realistic three-

dimensional image reconstruction by angular tiling," *Journal of Electronic Imaging*, vol. 23, no. 2, p. 023016, 2014.

[78] K. Wakunami and M. Yamaguchi, "Calculation for computer generated hologram using ray-sampling plane," *Optics express*, vol. 19, no. 10, pp. 9086–9101, 2011.

[79] S. Hamann, L. Shi, O. Solgaard, and G. Wetzstein, "Time-multiplexed light field synthesis via factored wigner distribution function," *Optics letters*, vol. 43, no. 3, pp. 599–602, 2018.

[80] J.-H. Park and M. Askari, "Non-hogel-based computer generated hologram from light field using complex field recovery technique from wigner distribution function," *Optics express*, vol. 27, no. 3, pp. 2562–2574, 2019.

[81] N. Padmanaban, Y. Peng, and G. Wetzstein, "Holographic near-eye displays based on overlap-add stereograms," *ACM Transactions on Graphics*, vol. 38, no. 6, pp. 1–13, 2019.

[82] M. Guizar-Sicairos and J. R. Fienup, "Phase retrieval with transverse translation diversity: a nonlinear optimization approach," *Optics express*, vol. 16, no. 10, pp. 7264–7278, 2008.

[83] R. W. Gerchberg, "Phase determination for image and diffraction plane pictures in the electron microscope," *Optik (Stuttgart)*, vol. 34, p. 275, 1971.

[84] G. Zheng, R. Horstmeyer, and C. Yang, "Wide-field, high-resolution fourier ptychographic microscopy," *Nature photonics*, vol. 7, no. 9, p. 739, 2013.

[85] J.-H. Park, J. Kim, and B. Lee, "Three-dimensional optical correlator using a sub-image array," *Optics express*, vol. 13, no. 13, pp. 5116–5126, 2005.

[86] Z. Li, J. Zhang, X. Wang, and D. Liu, "High resolution integral holography using fourier ptychographic approach," *Optics express*, vol. 22, no. 26, pp. 31935–31947, 2014.

[87] X. Ou, G. Zheng, and C. Yang, "Embedded pupil function recovery for fourier ptychographic microscopy," *Optics express*, vol. 22, no. 5, pp. 4960–4972, 2014.

[88] D. Armitage, I. Underwood, and S.-T. Wu, *Introduction to microdisplays*, vol. 11. John Wiley & Sons, 2006.

[89] L. J. Hornbeck, "Multi-level digital micromirror device," Dec. 10 1996. US Patent 5,583,688.

[90] T. Mishina, M. Okui, and F. Okano, "Viewing-zone enlargement method for sampled hologram that uses high-order diffraction," *Applied optics*, vol. 41, no. 8, pp. 1489–1499, 2002.

[91] G. Li, J. Jeong, D. Lee, J. Yeom, C. Jang, S. Lee, and B. Lee, "Space bandwidth product enhancement of holographic display using high-order diffraction guided by holographic optical element," *Optics express*, vol. 23, no. 26, pp. 33170–33183, 2015.

[92] J. Roh, K. Kim, E. Moon, S. Kim, B. Yang, J. Hahn, and H. Kim, "Full-color holographic projection display system featuring an achromatic fourier filter," *Optics express*, vol. 25, no. 13, pp. 14774–14782, 2017.

[93] H. Kim and B. Lee, "Optimal nonmonotonic convergence of the iterative fourier-transform algorithm," *Optics letters*, vol. 30, no. 3, pp. 296–298, 2005.

[94] F. Wyrowski, "Diffractive optical elements: iterative calculation of quantized, blazed phase structures," *JOSA A*, vol. 7, no. 6, pp. 961–969, 1990.

[95] C. B. Elliott, T. Credelle, S. Han, M. Im, M. Higgins, and P. Higgins, "Development of the pentile matrix$^{TM}$ color amlcd subpixel architecture and rendering algorithms," *Journal of the Society for Information Display*, vol. 11, no. 1, pp. 89–98, 2003.

[96] C. H. B. Elliott, M. F. Higgins, S. Hwang, S. Han, A. Botzas, B.-S. Hsu, M. Im, and S. Nishimura, "72.1: Invited paper: Pentile rgbw color processing," *SID symposium digest of technical papers*, vol. 39, no. 1, pp. 1112–1115, 2008.

# Appendix

Portions of the work discussed in this dissertation were also presented in the following publications:

[Chapter 3] J. Cho, S. Kim, S. Park, B. Lee, and H. Kim, “Dc-free on-axis holographic dis-play using a phase-only spatial light modulator,”Optics letters, vol. 43, no. 14,pp. 3397–3400, 2018.

# 초 록

본 박사학위 논문에서는 시스템의 부피를 최소화하면서, 시스템의 공간대역폭을 확장할 수 있는 새로운 다층 홀로그래픽 디스플레이 구조에 대해 논한다. 저해상도 공간광변조기를 광축 방향으로 적층하면 디스플레이의 크기를 최소화할 수 있을 뿐 아니라 변조기의 베젤로 인한 공백 문제를 최소화할 수 있다. 다층 홀로그래픽 디스플레이의 향상된 공간대역폭을 위해 컴퓨터 생성 홀로그램을 최적화 시키는 방법을 제안한다. 다층 홀로그래픽 디스플레이를 위한 컴퓨터 생성 홀로그램은 직접적으로 계산하는 것이 어렵기 때문에 최적화를 통해 계산한다. 제안된 최적화 방법은 공간광변조기의 변조 방법이나 그 수에 관계없이 적용할 수 있다. 다층 홀로그래픽 디스플레이가 다수의 공간광변조기를 이용하여 공간대역폭을 실질적으로 향상시킬 수 있음을 시뮬레이션을 통해 검증한다. 다층 홀로그래픽 디스플레이를 위한 초고해상도 컴퓨터 생성 홀로그램 고속 생성 알고리즘을 제안한다. 푸리에 타이코그래피 방법을 통해 초고해상도, 초고화질의 컴퓨터 생성 홀로그램을 기존의 방법에 비해 빠르게 계산할 수 있음을 보인다. 내장 동공 함수 복원 기술을 이용하여 계산량을 줄일 수 있음을 보이고, 통합 경사하강법을 통해 기존의 반복적 푸리에 변환 알고리즘의 수렴성을 향상시킬 수 있음을 보인다. 또한 기존의 반복적 푸리에 변환 알고리즘으로 최적화하기 어려운 위상 홀로그램 최적화 문제를 제안된 알고리즘으로 최적화가 가능함을 보인다. 실험과 시뮬레이션을 통해 제안된 알고리즘이 기존의 방법에 비해 홀로그램의 품질과 계산속도에서 장점이 있음을 검증한다. 다층 홀로그래픽 디스플레이에 내재된 노이즈를 제거할 수 있는 컴퓨터 생성 홀로그램의 최적화 방법에 대해 논한다. DC 노이즈를 제거하기 위해 추가 광학계가 필요없고, 에너지 손실을 최소화할 수 있는 다층 구조의 축 홀로그래피 광학 시스템을 제안하고, 이를 위한 컴퓨터 생성 홀로그

램의 최적화 알고리즘을 제안한다. 실험을 통해 제안된 시스템과 알고리즘이 DC 노이즈를 효과적으로 차단할 수 있음을 검증한다. 또한 특수한 서브픽셀 구조를 지닌 광공간변조기를 위해 컴퓨터 생성 홀로그램을 보정하는 방법을 제안한다. 제안된 알고리즘은 임의의 서브픽셀 구조에 대해 모두 적용이 가능하며, 다층 디스플레이에서의 픽셀 정렬 문제에도 적용이 가능하다.

**주요어**: 홀로그래픽 디스플레이, 컴퓨터 생성 홀로그램, 공간대역폭, 반복적 푸리에 변환 알고리즘, 디지털 홀로그래피

**학번**: 2013-20888